Remote Sensing Applications: Society and Environment 38 (2025) 101528

Contents lists available at ScienceDirect

Remote Sensing Applications: Society and Environment

journal homepage: www.elsevier.com/locate/rsase

Development of topo-bathymetric continuum profiles for coastal barriers with global open-access data

Valeria Fanti [a,*], Carlos Loureiro [a,b], Óscar Ferreira [a]

[a] Centre for Marine and Environmental Research (CIMA/ARNET), Universidade do Algarve, Faro, 8005-139, Portugal
[b] Geological Sciences, School of Agricultural, Earth and Environmental Sciences, University of KwaZulu-Natal, Durban, 4001, South Africa

ARTICLE INFO

Keywords:
Barrier profiles
Global models
Satellite topography
Nearshore bathymetry
Coastal hazards

ABSTRACT

Coastal barriers are dynamic and vulnerable coastal environments exposed to storms and rising sea levels, requiring a thorough understanding of their physical and geomorphological characteristics. Despite this, high-resolution topo-bathymetric data are not openly available for most of the world's coastal areas, preventing accurate estimation of the exposure to storms and associated risks. Global models of topography and bathymetry, derived from remote sensing techniques, are available worldwide as an open-source solution to characterise coastal morphology. However, their coarse resolution, limited vertical and horizontal accuracy, alongside inconsistencies in the transition from land to the shallow nearshore zone, make their use in coastal areas challenging, requiring careful evaluation. This study investigates the potential and limitations of four recent open-access satellite-derived topographic models (Copernicus GLO-30 DEM, AW3D30, TanDEM-X, Euro-Maps 3D) and three bathymetric models (GEBCO_2023, SRTM15+, ETOPO 2022) in five coastal barriers. It proposes a new approach to integrate global models to provide a consistent representation of the topo-bathymetric continuum profile in coastal areas characterised by a barrier morphology. Coastal barrier profiles, representative of natural sectors and characterized by morphological homogeneity, were derived by merging global topographic and bathymetric digital elevation models and implementing an equilibrium profile in the transition zone. The profiles obtained from the global models were compared with higher resolution local or regional topo-bathymetry. The global topographies tend to underestimate the dune top, with TanDEM-X giving the best results in terms of dune crest height and beach slope. The barrier continuum profiles that merged TanDEM-x and ETOPO 2022 global models were found to have the lowest error, with a vertical RMSE of 0.76 m. Based on integration of these remotely sensed models, it is possible to determine average representative coastal barrier profiles suitable for use in global to regional coastal studies or in data-poor areas, potentially serving as a cost-effective tool for preliminary coastal hazard assessments and early warning systems at wide spatial scales.

1. Introduction

Coastal barriers are dynamic, valuable, yet vulnerable coastal environments (e.g., McBride et al., 2022), and are strongly affected by storm events and sea level rise (e.g., Gharagozlou et al., 2020; Irish et al., 2010). To understand and model their morphological response to coastal processes, it is necessary to characterise not only the forcing agents but also the geomorphological properties of

* Corresponding author.
E-mail address: vfanti@ualg.pt (V. Fanti).

https://doi.org/10.1016/j.rsase.2025.101528
Received 26 July 2024; Received in revised form 27 February 2025; Accepted 18 March 2025
Available online 20 March 2025

these coastal systems (Cooper et al., 2018). Such properties are also paramount for the definition of morphological geo-indicators (see Carapuço et al., 2016) or process-based indicators (Ferreira et al., 2017), which can be used in coastal hazard and risk assessments (e.g. Torresan et al., 2008; Nguyen et al., 2016). Several methods have been developed to derive high-resolution land topography and ocean bathymetry data at local scales (see Melet et al., 2020) and to extract coastal barrier characteristics (Wernette et al., 2016). These include airborne Light Detection and Ranging (LiDAR), structure from motion photogrammetry using imagery from unmanned aerial vehicles and multibeam echo sounding. However, high-resolution topo-bathymetry is still not available in many coastal areas around the world (e.g., Archer et al., 2018; Simpson et al., 2015; Wechsler, 2007), and there is a global lack of data in intertidal and shallow water coastal regions (Tseng et al., 2017). This is particularly relevant in areas where water clarity is suboptimal and wave breaking restricts direct surveying. Moreover, data collected in coastal waters are often under national jurisdiction, outdated, and not openly available (Wölfl et al., 2019). Despite major international seafloor mapping initiatives (e.g. SEABED, 2030; EMODnet, ETOPO), more than fifty percent of the world's coastal waters shallower than 200 m depth remain unsurveyed (IHO, 2023), with less than 10 % of the seafloor covered by high-resolution multibeam data (Mayer et al., 2018), mostly collected in economically relevant areas and often confidential (Wölfl et al., 2019).

Given these limitations, Global Digital Elevation Models (GDEMs) and Global Bathymetric Models (GBMs), generated using remote sensing techniques, are increasingly becoming the data of choice for many coastal applications from global to local scales. The first GDEM was produced in 2003 by the Shuttle Radar Topography Mission (SRTM, Farr et al., 2007), with 90 m horizontal resolution, after which several open source GDEMs options derived from Synthetic Aperture Radar (SAR) technologies or optical satellite imagery became available (Hawker et al., 2018a; Proietti et al., 2017). Between 2009 and 2020 several 30 m resolution GDEMs were released: the Advanced Spaceborne Thermal Emission and Reflection Radiometer (ASTER, Yamaguchi et al., 1998), the NASADEM derived from reprocessing and improving SRTM (Crippen et al., 2016), the World3D based on stereo-imagery from the Advanced Land Observing Satellite (ALOS) (AW3D30, Tadono et al., 2016), the SAR-derived TanDEM-X (Rizzoli et al., 2017) and, from the TanDEM-X terrain correction and hydrological editing, the Copernicus GLO-30 DEM (Fahrland et al., 2020). Recently, commercial GDEMs have also been developed, generally with a higher spatial resolution and better accuracy, such as the CoastalDEM (Kulp and Strauss, 2019) at 30m resolution, WorldDEM (i.e. the commercial TanDEM-X) at 12 m resolution, the stereo-derived Euro-Maps 3D (Uttenthaler et al., 2013) at 5 m resolution and Vricon at 0.5 m resolution.

Regarding global ocean bathymetry and starting in the mid-1990s with Smith and Sandwell (1994, 1997), the advent of satellite altimetry led to major advances in the estimation of bathymetry from space to complement the sparse and scarce high-resolution bathymetric surveys (Wölfl et al., 2019). Since then, several GBMs obtained from satellite-derived gravity anomalies, integrated with marine remote sensing techniques (single and multibeam echo sounding, bathymetric LiDAR) and existing nautical charts have been produced using a range of interpolation techniques, and released at increasingly higher resolutions (Tozer et al., 2019). The most recent GBMs are SRTM15+V2.0 Tozer et al. (2019); ETOPO 2022 (NOAA National Centers for Environmental Information, 2022) and GEBCO_2023 (GEBCO Bathymetric Compilation Group, 2023), all providing global coverage on a 15 arcsecond grid (~460 m). Despite providing elevation data for land and depth data for the ocean, bathymetry and topography in these GBMs are not merged but rather separated by the shoreline boundary, defined using The Global Self-consistent, Hierarchical, High-resolution Geography Database (GSHHG) for SRTM15+V2.0 and ETOPO 2022 or the World Vector Shorelines (WVS) dataset for GEBCO_2023. This can result in a misalignment in the order of a few hundred meters (Tozer et al., 2019), which, together with their coarser resolution than openly available GDEMs, makes GBMs use challenging for nearshore and coastal areas.

Despite years of progress and increasing vertical and horizontal accuracies, GDEMs still have systematic to random errors (Hawker et al., 2018a) with various authors pointing to the need for up-to-date, openly available and high-resolution GDEMs (Hawker et al., 2018a; Schumann and Bates, 2018; Simpson et al., 2015). The current GDEMs are considered to be uncertain in terms of vertical accuracy for high-confidence evaluations of sea level rise and coastal flooding impacts (Gesch, 2018), leading to errors in coastal hazard assessments (Melet et al., 2020; Serafin et al., 2019) and underestimation of coastal vulnerability (Kulp and Strauss, 2016; Parodi et al., 2020; Simpson et al., 2015). Similarly, global compilations of ocean bathymetry are still incomplete (Li et al., 2023), have insufficient vertical and spatial resolution, interpolation errors, and inaccuracies in shallow waters (Cesbron et al., 2021). Moreover, their vertical consistency is seldom guaranteed when merging multiple data sources (GEBCO Bathymetric Compilation Group, 2023) due to the lack of detailed information on the vertical datums (Weatherall et al., 2015). Therefore, it is crucial to recognise their limitations, errors, and inconsistencies but also to develop approaches to improve their quality and guarantee a suitable use as openly available global databases are an advantageous alternative to costly and sparsely available high-resolution data sources, particularly in remote and/or data poor regions where more accurate local data is not available and collection is not feasible. Careful evaluation of GDEMs and GBMs is required to ensure appropriate consideration of data uncertainties, especially in coastal areas where more detailed and accurate information is fundamental for effective management and decision-making (Gesch, 2018; Parodi et al., 2020; Sepúlveda et al., 2020; Simpson et al., 2015), and where remote sensing techniques present greater challenges.

Although better remote sensing solutions for estimating bathymetry in coastal areas are beginning to emerge both locally (Bergsma et al., 2021; Caballero and Stumpf, 2019; Cesbron et al., 2021; Li et al., 2023; Pacheco et al., 2015; Pleskachevsky et al., 2011), regionally (Bishop-Taylor et al., 2019) and globally (Almar et al., 2021a; Ashphaq et al., 2021; Salameh et al., 2019), as well as algorithms for editing and improving GDEMs (González et al., 2020; Hawker et al., 2018a, 2018b), global models are still commonly used without fully acknowledging their inaccuracies and errors or requiring in-situ data for calibration. In particular, GBMs have been used without corrections to assess tsunami hazards (Sepúlveda et al., 2020), storm surges and extreme sea levels (Muis et al., 2020), shoreline retreat due to sea level rise (Vousdoukas et al., 2020), and coastal flooding (Parodi et al., 2020). Similarly, space-borne GDEMs have been widely applied in coastal areas for hydrogeomorphological risk assessment and damage estimation for natural hazards such as coastal flooding and inundation (Archer et al., 2018; Gesch, 2018; Hawker et al., 2018a, 2018b; Mason et al., 2015,

2016; Neumann et al., 2015; Vousdoukas et al., 2016, 2018), also considering the effect of sea level rise (Almar et al., 2021b; Bove et al., 2020; Fandé et al., 2022; Gesch, 2018; Kulp and Strauss, 2019; Parodi et al., 2020; Vousdoukas et al., 2022). Results from such analyses have been incorporated in key findings in the IPCC Sixth Assessment Report (IPCC, 2022). A fundamental challenge for the correct use of GDEMs and GBMs is to understand and quantify their errors and then, as they propagate through the analysis, incorporate these uncertainties into the models and projections (Bove et al., 2020; Leon et al., 2014; Sepúlveda et al., 2020; Vousdoukas et al., 2018). Moreover, it is also necessary to develop tools and methods that minimise errors and allow the definition of representative coastal profiles from GDEMs and GBMs that are suitable for coastal hazard and risk analysis. This paper presents a new approach to determine continuous topo-bathymetric barrier profiles from GDEMs and GBMs and proposes a novel solution to minimise the challenges associated with the absence of shallow nearshore and intertidal data, robustly evaluating the performance for estimating coastal barrier profiles. These profiles can be widely applied in regional to global scale analysis that evaluate the vulnerability of coastal barriers to coastal hazards, as well as in impact and disaster risk reduction assessments for present and future scenarios.

2. Materials and methods

2.1. Topography

In this work, four recent openly available satellite-derived GDEMs were selected with the criteria of having a minimum resolution of 30 m to resolve the coastal barrier morphology. In particular, the following GDEMs were analysed: Copernicus GLO-30 DEM (Fahrland et al., 2020) and AW3D30 (Tadono et al., 2014) with 30 m resolution, TanDEM-X (Rizzoli et al., 2017) with 12 m resolution and Euro-Maps 3D with 5 m resolution (Uttenthaler et al., 2013) (Table 1). Euro-Maps 3D is derived from IRS-P5 CartoSat-1 in-flight stereo data and was selected because it is the highest resolution GDEM, although with a free download for Copernicus-related institutional users limited to an area of 1400 km^2, which limited the availability across the study sites. The TanDEM-X GDEM was generated using SAR interferometry and allows for more accurate topographic data by measuring the phase differences between multiple SAR acquisitions from two satellites (TerraSAR-X and TanDEM-X) and is openly available at 12 m for non-commercial research purposes. TanDEM-X has been shown to outperform previously commonly used GDEMs, such as ASTER, SRTM and AW3D30, in terms of accuracy in a wide variety of areas such as mountainous, coastal, urban and vegetated (Chu and Lindenschmidt, 2017; Gdulová et al., 2021; Gesch, 2018; Li et al., 2021; Parodi et al., 2020; Vassilaki and Stamos, 2020). The Copernicus GLO-30 DEM was derived from TanDEM-X after terrain correction and hydrological processing by removing spikes, gap filling and identifying systematic and random errors (Collins et al., 2015), thus representing an improvement to the native TanDEM-X (Marešová et al., 2021), although it has lower horizontal resolution (Table 1). Finally, AW3D30 was derived from images acquired by the panchromatic remote sensing instrument for stereo mapping onboard of the ALOS and it proved to be a robust and accurate DEM for multiple geographic regions (Uuemaa et al., 2020) and specifically for maximum coastal elevations (Almar et al., 2021b).

All GDEMs analysed represent the actual surface of the terrain (i.e. they are digital surface models), including infrastructures and vegetation. Since the main objective of this work is to define the uncertainties of the models for coastal barriers, only natural areas were selected, avoiding heavily vegetated or built-up areas. The analysis was performed on five natural coastal barriers sectors specifically, the Ria Formosa in Portugal, Pamlico Sound and Fire Island in the USA, Terschelling in the Netherlands, and Myalup in Australia (see section 2.3 for details of study sites), for which high-resolution LiDAR-derived DEMs were also available (Table 2).

Table 1
Specifications for global topographic models.

GDEMs	Pixel Spacing	Horizontal Datum	Vertical Datum	Absolute Horizontal Accuracy[a]	Absolute Vertical Accuracy[b]	Relative Vertical Accuracy	Acquisition window	Coverage
TanDEM-X	0.4 arcsec (~12 m @ equator)	WGS84-G1150 EPSG:4979	WGS84-G1150 ellipsoid	<10m	<10m	2m (slope ≤ 20 %) 4m (slope >20 %)	2010–2015	Global (−180°W to 180°E, −90°S to 84°N)
Copernicus GLO-30 DEM	1 arcsec (~30 m @ equator)	WGS84-G1150 EPSG:4326	EGM2008 EPSG:3855	<6m	<4m	<2m (slope ≤ 20 %) <4m (slope >20 %)	2010–2015	Global (−180°W to 180°E, −90°S to 90°N)
Euro-Maps 3D	5 m	WGS84 EPSG:4326	EGM96	5–10 m	5–10 m	<3m	2007–2016	Global, cloud limited (Proietti et al., 2017)
AW3D30	1 arcsec (~30 m @ equator)	WGS84 EPSG:4326	EGM96	7 m	7 m	5m RMSE	2006–2011	Global, gap filled (Takaku et al., 2020)

a 90 % circular error (CE90)

b 90 % linear error (LE90)

2.2. Bathymetry

Among all the available GBMs, the most recent and commonly used were analysed in this work and include SRTM15+ (Tozer et al., 2019), GEBCO_2023 (GEBCO Bathymetric Compilation Group, 2023; ETOPO 2022 (NOAA National Centers for Environmental Information, 2022) (Table 3). These were compared with high-resolution LiDAR-derived bathymetric DEMs to approximately 10 m water depth and, at greater depths, with regional bathymetric models (RBMs) such as the CUDEM for the USA (Amante et al., 2023), EMODnet for Europe (Thierry et al., 2019) and the 2023 Australian Bathymetry and Topography grid (Beaman, 2023) (Table 4). The SRTM15+ bathymetry was developed following the methodology outlined by Smith and Sandwell (1997, 1994) and has recently been augmented in shallow areas with bathymetric datasets developed by the Seabed 2030 Regional Centers for the production of GEBCO Bathymetric Compilation Group, 2023. The GEBCO_2023 grid is augmented through a blending "remove-restore" procedure (Weatherall et al., 2015) with SRTM15+ and regional bathymetric datasets based on multibeam, singlebeam and other individual surveys from EMODnet and additional sources. ETOPO 2022 integrates bathymetric data from GEBCO Bathymetric Compilation Group, 2023 and GMRTv4.0, as well as land topography from Copernicus GLO-30 and other data sources (NOAA National Centers for Environmental Information, 2022). The RBMs also include GBMs, for instance, ETOPO and SRTM are incorporated in the Australian RBM in areas where higher resolution sounding data are not available (Whiteway, 2009), GEBCO in EMODnet (Thierry et al., 2019) and SRTM15+ in CUDEM (Amante et al., 2023).

While these datasets are related and have interdependencies due to shared high-resolution data, their comparison is important to consistently assess their accuracy and performance in different coastal areas. The fact that they are derived from the assimilation of heterogeneous data types has implications in terms of vertical datum, as surface models in shallow water areas are often assumed to be referred to MSL, even when they have distinct vertical references (GEBCO Bathymetric Compilation Group, 2023; NOAA National Centers for Environmental Information, 2022). The GEBCO_2023 grid is accompanied by a Type Identifier file (TID, GEBCO Bathymetric Compilation Group, 2023) while each ETOPO 2022 tile has an associated Source ID (SID, NOAA National Centers for Environmental Information, 2022) with information on the source data merged into the final grid. However, detailed information on each specific dataset used and the vertical datum are unavailable.

To evaluate the accuracy of the GBMs and RBMs, detailed bathymetry was extracted at each site from LiDAR-derived DEMs (Table 4). For the study sites in the USA and Australia, multibeam data were available and integrated with the LiDAR data, while for the other sites the GBMs could only be compared with LiDAR-derived DEMs down to 10 m water depths due to the lack of high-resolution offshore surveys, and with RBMs for deeper parts of the profiles.

2.3. Study sites

Coastal barriers are accumulations of unconsolidated sediments deposited by waves, tides and wind occurring along ocean coastlines that act as important natural buffers against coastal hazards (McBride et al., 2022). They are valuable coastal environments but because they are at the land-water interface, data from satellite sensors in these areas are subject to greater uncertainty. Five coastal barriers were selected from diverse locations around the world (Fig. 1), namely the Ria Formosa in southern Portugal, the Outer Banks and Fire Island in the USA, Terschelling in the Netherlands, and Myalup in Australia. This selection was made based on the availability of high resolution and accurate topo-bathymetric data, but also to include systems with complex morphology associated with different oceanographic and atmospheric forcing (i.e. wind intensity, wave energy and tidal range). All sites are wave-dominated natural coastal barriers with a semi-diurnal mesotidal regime, with Faro and Terschelling presenting a few houses in the backbarrier area that were avoided when extracting the profiles. The GDEMs and GBMs were evaluated at these diverse coastal barrier sites to assess their performance and accuracy in capturing complex topo-bathymetric features. The barrier sections analysed extended from the barrier area behind the primary dune to an offshore depth of approximately 30 m below mean sea level.

2.4. Horizontal and vertical datum correction

To ensure a consistent comparison of the datasets, the GDEMs and GBMs (Tables 1 and 3) were reprojected to the horizontal datum of the high-resolution data (Tables 2 and 4). The vertical datums for the DEMs in the USA were corrected using the National Oceanic and Atmospheric Administration (NOAA) Vertical Datum Transformation VDatum software version v4.4.2, in the Netherlands using the RDNAPTRANS 2018 parameters in combination with PROJ6, in Australia with the AUSGeoid2020 and in the Ria Formosa with the local mean sea level from the openly available dataset by Cyrille et al. (2021). Whilst it is not possible to quantify the vertical uncertainty resulting from the datum conversion, this error is incorporated into the overall error analysis of the topo-bathymetric profiles.

2.5. Cleaning of spikes and water bodies removal

A preliminary analysis was carried out across entire sectors of the coastal barriers to detect gaps and remove inaccuracies and spikes. A visual inspection of the spikes against ESRI satellite imagery revealed that most spikes were located near water bodies or associated with the presence of buildings in backbarrier areas (for Faro and Terschelling). In the case of buildings, even if these were avoided through the careful selection of profile locations, their influence can still affect the surrounding area due to the coarse resolution of the GDEMs. The Euro-Maps 3D, Copernicus GLO-30 and AW3D30 datasets have already been processed with gap filling and error detection algorithms (Marešová et al., 2021; Takaku et al., 2020) and didn't require further correction. However, TanDEM-X presented several spikes, mostly at the ocean-land interface, and these were manually removed (Fig. 2). The Water Indication Mask

Table 2
Specifications for local topographic models.

Location	Local DEM	Pixel Spacing	Horizontal Datum	Vertical Datum	Absolute Horizontal Accuracy[a]	Absolute Vertical Accuracy[b]	Acquisition window
Faro, Portugal	LiDAR 2011	2 m	PT-TM06/ETRS89 EPSG:3763	Cascais Helmert 38, GeodPT08	RMSE 0.16 m (Direcção-Geral do Território, 2011)		November/ December 2011
Outer Banks, USA	2019 USACE NCMP Topobathy Lidar DEM: East Coast (NC)	1 m	EPSG:3631 NAD83 (2007)	NAVD88	100 cm (95 % confidence level)	20 cm (95 % confidence level)	2019
Fire Island, USA	2020 USACE NAN Topobathy Lidar DEM: New Jersey and New York	1 m	EPSG:6318 NAD83(2011)	EPSG:5703 NAVD88	100 cm (95 % confidence level)	20 cm (95 % confidence level)	2012
Terschelling, Netherlands	AHN3	0.5 m	EPSG:28992 - Amersfoort/ RD New Ellipsoid: Bessel 1841	EPSG:5709 NAP height (Normaal Amsterdams Peil)	objects of 2 x 2 m have a maximum position deviation of 50 cm (PDOK L., 2017)	Standard deviation <15 cm for 99.7 % of points (PDOK L., 2017)	2014–2019
Myalup, Australia	LiDAR DEM	5 m	EPSG:4283 GDA94	AHD – using AUSGeoid98	80 cm (95 % confidence interval)	30 cm (95 % confidence interval)	2001–2015

[a] 90 % circular error (CE90)
[b] 90 % linear error (LE90)

Table 3
Specifications for global and regional bathymetric models.

GBMs	Pixel Spacing	Horizontal Datum	Vertical Datum	Accuracy	Acquisition window	Coverage
GEBCO_2023	15 arcsec (~460 m @ equator)	WGS84 EPSG:4326	MSL	Multiple data contributors (https://www.gebco.net/about_us/acknowledgements/our_data_contributors/)		Global (–89° 59' 52.5''N to 89° 59' 52.5''S, 179° 59' 52.5''W to 179° 59' 52.5''E)
SRTM15+V2.0	15 arcsec (~460 m @ equator)	WGS84 EPSG:4326	EGM96 EPSG:5171	RMSE ±150 m in the deep oceans and ±180 m near coasts (Tozer et al., 2019)	Multiple data contributors (Table 2, Tozer et al., 2019)	Global –(-180°W to 180°E, −90°S to 90°N)
ETOPO 2022	15 arcsec (~460 m @ equator)	WGS84 EPSG:4326	EGM2008	Multiple data contributors (NOAA National Centers for Environmental Information, 2022)		Global –(-180°W to 180°E, −90°S to 90°N)
RBMs	**Pixel Spacing**	**Horizontal Datum**	**Vertical Datum**	**Accuracy**	**Acquisition window**	**Coverage**
NCEI's Continuously Updated DEM (CUDEM)	1/9th-1/3rd arcsec (~3–10 m @ equator)	EPSG:4269 NAD83	NAVD88	Horizontal accuracy: 100 cm Vertical accuracy: 50 cm	Multiple data contributors (Amante et al., 2023)	–U.S. Atlantic; Gulf of Mexico Coasts; portions of Alaska, Washington, Oregon and California Coasts; Hawaii; Guam and –Commonwealth of the Northern Mariana Islands; Puerto Rico and U.S. Virgin Islands; American Samoa (Amante et al., 2023)
EMODnet Bathymetry World Base Layer	115 m	WGS84 EPSG:4326	MSL	Multiple data contributors (Thierry et al., 2019)		Europe (36°W to 43°W, 15°N to 90°N)
Australian Bathymetry and Topography 2023	250 m	WGS84 EPSG:4326	MSL	Multiple data contributors (Beaman, 2023)		Australia (92°E to 172°E, −8°S to −60° S)

included in the TanDEM-X auxiliary files (Wendleder et al., 2012; Wessel, 2018) was used to remove water bodies from the GDEM, excluding pixels with a low interferometric coherence (mask values greater than 33) from the analysis. For Euro-Maps 3D, Copernicus GLO-30 and AW3D30, the water pixels were already flagged as zero.

2.6. DEM resampling

To better compare the cross-shore profiles of the coastal barriers, all GDEMs and GBMs were resampled using the QGIS SAGA "Resampling" tool to match the LiDAR's resolution and obtain a smoother profile. A bilinear interpolation method was tested using a weighted average of the nearest 4 cells, alongside a bicubic spline interpolation, which fits a smooth curve through the nearest 16 cell centers, and a B-spline interpolation, which is a smooth surface passing through the input points, minimizing the total curvature. Previous studies on spatial interpolation methods for DEMs have shown that higher-order interpolation methods, such as bicubic and biquadratic (Kidner, 2003; Shi et al., 2005, 2014) or spline (Her et al., 2015), are more accurate than bilinear interpolation. However, other authors suggested that case-specific interpolation methods should be employed (El-Quilish et al., 2018; Smith et al., 2004). The differences in the DEMs obtained from the three interpolation methods tested at the sites of interest were not relevant, and the bilinear method was chosen because of its better performance when compared to the LiDAR data.

2.7. Error metrics

The vertical error of the GDEMs and GBMs was evaluated by subtracting the LiDAR-derived reference elevation (h_{LiDAR}) from the topographic or bathymetric DEM (h_{DEM}) at each pixel (i) along a ~2 km natural sector of the coastal barriers (1 km for Praia de Faro due to the presence of buildings):

$$\Delta h_i = h_{i,LiDAR} - h_{i,DEM} \tag{1}$$

The vertical accuracy of the GDEMs and GBMs was assessed using the root mean square error (RMSE), Pearson's correlation coefficient (R), standard deviation (STD), mean absolute error (MAE), bias and the linear error at the 90th percentile (LE90), calculated as:

$$RMSE = \sqrt{\frac{1}{N}\sum_{i=1}^{N}\Delta h_i^2} \tag{2}$$

Table 4
Specifications for local bathymetric models (N/A where not available).

Location	Local DEMs	Pixel Spacing	Horizontal Datum	Vertical Datum	Horizontal Accuracy	Vertical Accuracy	Acquisition window
Faro, Portugal	LiDAR 2011	2 m	PT-TM06/ ETRS89 EPSG:3763	Cascais Helmert 38, GeodPT08	<5 m + 5 % of depth (IHO, 2022, 1a)	RMSE 30 cm (DGT, 2011)	June/August 2011
Outer Banks, USA	2019 USACE NCMP Topobathy Lidar DEM: East Coast (NC)	1 m	EPSG:3631 NAD83 (NSRS, 2007)	NAVD88	100 cm at 95 % confidence level	$\sqrt{0.25^2 + (0.0075d)^2}$ m at 95 % confidence level (d is depth)	2019
	NOAA/NCEI Multibeam bathymetry mosaic (Varner et al., 2017)	3 arcsec (~90 m @ equator)	WGS84 EPSG:4326	MSL	N/A	N/A	Multiple dates (from 1998 to 2020)
Fire Island, USA	2020 USACE NAN Topobathy Lidar DEM: New Jersey and New York	1 m	EPSG:6318 NAD83(2011)	EPSG:5703 NAVD88	$3.5 + 0.05*d$ m at 95 % confidence level	$\sqrt{0.25^2 + (0.0075d)^2}$ m at 95 % confidence level (d is depth)	2020
	NOAA/NCEI Multibeam bathymetry mosaic	3 arcsec (~90 m @ equator)	WGS84 EPSG:4326	MSL	N/A	N/A	Multiple dates (1993–2019)
Terschelling, Netherlands	Jarkus grid	5 m	EPSG:28992	NAP (Normaal Amsterdams Peil)	0.4 m (Wiegmann et al., 2002)	0.25 m (Wiegmann et al., 2002)	2020
Myalup, Australia	Multibeam Dataset of Australia (2018)	50 m	EPSG:7850	MSL	N/A	N/A	Multiple dates (1989–2018)

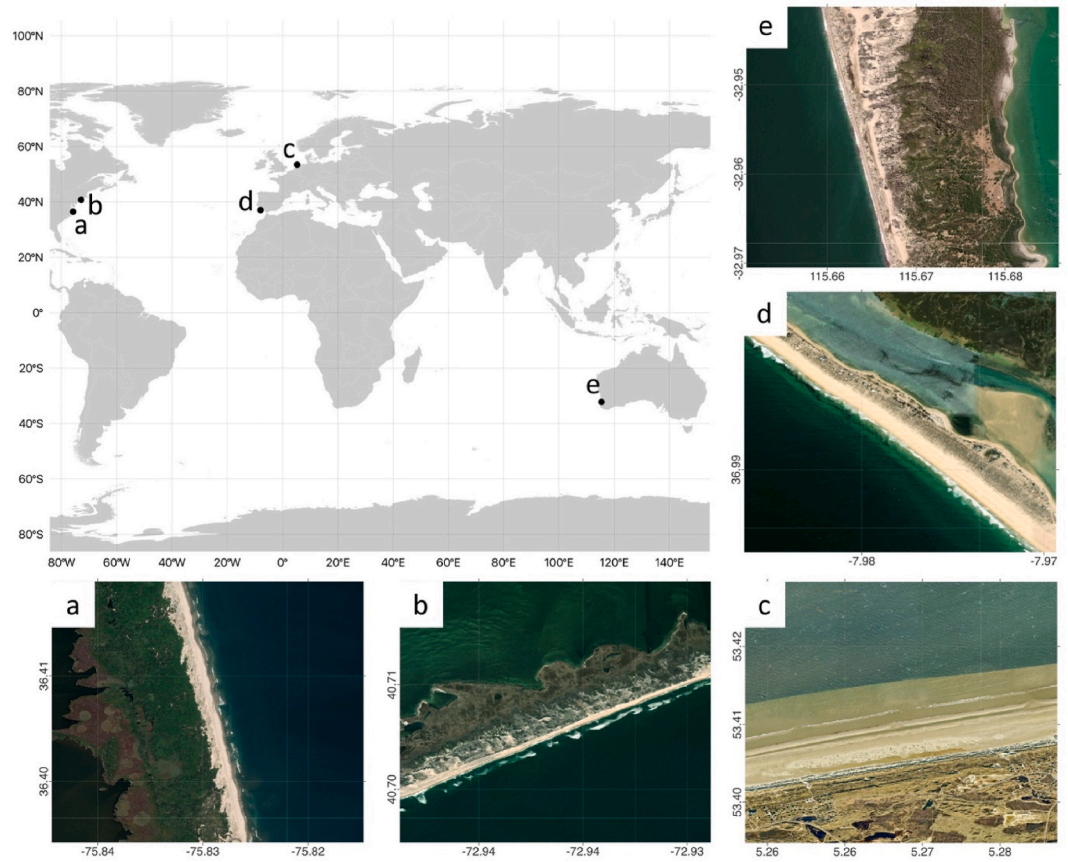

Fig. 1. Location of coastal barriers and analysed 2 km-long sectors in: a) the Outer Banks in the USA, b) Fire Island in the USA, c) Terschelling in the Netherlands, d) Ria Formosa in southern Portugal and e) Myalup in Australia. Source: ESRI World Imagery.

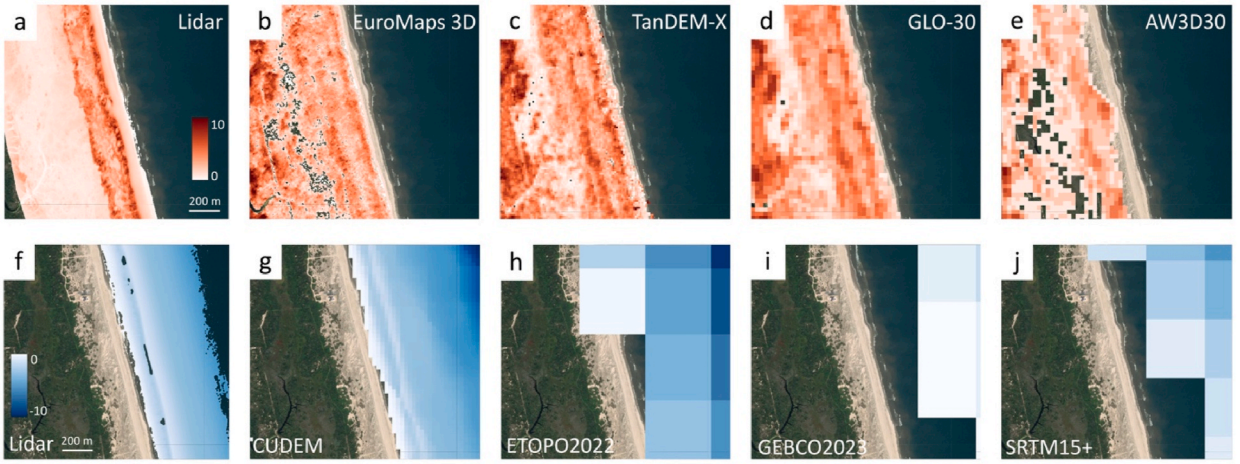

Fig. 2. Visualisation of topographic (a–e) and bathymetric (f–j) data at the Outer Banks, USA, displaying the different resolutions according to the data source. All GDEMs and GBMs are reprojected into the same horizontal (EPSG:3631 NAD83) and vertical (NAVD88) datum.

$$R = \sum_{i=1}^{N} \left(h_{i,LiDAR} - \overline{h_{i,LiDAR}}\right)\left(h_{i,DEM} - \overline{h_{i,DEM}}\right) \Bigg/ \sqrt{\sum_{i=1}^{N} \left(h_{i,LiDAR} - \overline{h_{i,LiDAR}}\right)^2 \sum_{i=1}^{N} \left(h_{i,DEM} - \overline{h_{i,DEM}}\right)^2} \tag{3}$$

$$STD = \sqrt{\frac{1}{N-1} \sum_{i=1}^{N} (\Delta h_i - ME)^2} \tag{4}$$

$$MAE = \frac{1}{N} \sum_{i=1}^{N} |h_{i,LiDAR} - h_{i,DEM}| = \frac{1}{N} \sum_{i=1}^{N} |\Delta h_i| \tag{5}$$

$$Bias = \frac{1}{N} \sum_{i=1}^{N} h_{i,LiDAR} - h_{i,DEM} = \frac{1}{N} \sum_{i=1}^{N} \Delta h_i \tag{6}$$

$$LE90 = Q_{|\Delta h|}(0.9) \tag{7}$$

where N is the total number of pixels considered when extracting the profiles from the LiDAR and the interpolated GDEMs and GBMs.

2.8. Merging of topo-bathymetry

After assessing the overall accuracy of the GDEMs and GBMs along a ~2 km natural sector of the coastal barriers, an area of ~300 m alongshore was selected for each site to extract cross-shore barrier profiles. These areas were defined as having homogeneous characteristics in terms of dune and beach morphology, and areas with either high (arboreal) vegetation or infrastructure (roads, walls or small buildings scattered among the natural dunes) were avoided. Along the natural areas selected, cross-shore profiles were extracted at 30 m intervals (chosen to match the resolution of the coarser GDEM), aligned at the dune crest (i.e. profile origin) and averaged to obtain a single profile representative of the selected area. After averaging, a local regression smoothing method (*LOESS interpolation*) was applied to preserve the peaks while smoothing any spike at the tails of the profiles. The bathymetry was also extracted along the same profiles, extending offshore to approximately 30 m water depth. To ensure spatial agreement between topographic and bathymetric datasets, the same horizontal shift used for aligning the topographic profiles to the dune crest was applied to the corresponding bathymetric profiles, and the GBMs and RBMs were also averaged into a single profile representative of the selected sector for each coastal barrier.

To merge the LiDAR-derived topographies with the RBMs, the most seaward intersecting point was chosen to prioritize the dataset with higher resolution, i.e. the LiDAR-derived topo-bathymetries. An equilibrium profile was then implemented to merge the topographic and bathymetric profiles, as there is high topographic variability in the upper shoreface and inaccurate or absent bathymetric information in the shallow nearshore area in the GDEMs and GBMs, respectively. The equilibrium profile was applied under the assumption that the selected areas have sufficient sediment supply and are in equilibrium conditions with the hydrodynamic forcing. The concept of an equilibrium profile configuration on sandy beaches was first developed by Bruun (1954) as a simple empirical relationship between the cross-shore profile depth (y) and the distance offshore from the shoreline (x), and later modified by Dean (1991):

$$y = Ax^{2/3} = 0.067^{*} w_s^{0.44} \tag{8}$$

where A is the sediment-dependent scale parameter obtained from the sediment fall velocity w_s, determined according to the median sediment grain size ($D50$) (Soulsby, 1997). The use of Dean's (1991) equilibrium profile has the advantage of simplicity as it depends on a single site-specific parameter, the $D50$, and it represents the concave-up nearshore shape typically found on wave-dominated barriers. However, due to the lack of sediment information in many coastal areas, in this case the Dean profile was derived by fitting the equilibrium curve from the mean sea level (z ~ 0) to the point where the GBM intersects the depth of closure (d_c). This is the depth beyond which the bottom changes and sediment transport become negligible at an annual scale, which Dean (2003) considered to be the limit of the equilibrium profile. For defining the d_c the formula proposed by Hallermeier (1981) for sandy beaches was used:

$$d_c = 2.28H_{12h/y} - 68.5\left(H_{12h/y}^2 \Big/ gT_{12h/y}^2\right) \tag{9}$$

where $H_{12h/y}$ is the significant wave height that is exceeded for 12 h per year (or the wave height with 0.137 % probability of occurrence in one year), $T_{12h/y}$ is the associated wave period and g is the acceleration of gravity. Wave data (significant wave height and peak period) were retrieved from the WAVERYS global wave reanalysis (Law-Chune et al., 2021) for the nearshore area of each study site. This reanalysis has a temporal resolution of 3 h for the years 1993–2021 and a spatial resolution of 0.2°x0.2°. The extracted significant wave heights were first calibrated to account for WAVERYS underestimation in coastal areas (Eq. (1) in Fanti et al., 2023). In this way, instead of first selecting a specific $D50$ value, which is often neither available nor clearly specified from where it was obtained in the field (Aragonés et al., 2016), and only then estimating the equilibrium profile, the depth of closure is used to determine the extent of the equilibrium profile and thus the A parameter in Eq. (8). The corresponding values of $D50$ were then compared to values retrieved from the literature (Table A.4, Athanasiou et al., 2021; CSE, 2015; Grasso et al., 2009; Kana et al., 2011; Kombiadou

et al., 2021; Pilarczyk et al., 1989; Poelhekke et al., 2016; Safak et al., 2017; Short, 2022; Splinter et al., 2014) to check plausibility of the result obtained and were considered acceptable if in the range of fine to medium sand (0.125 mm–0.5 mm, Wentworth, 1922).

3. Results

3.1. Evaluation of GDEMs' elevation accuracy

The vertical errors of the GDEMs were assessed across the study sites and showed varying levels of accuracy compared to the high-resolution DEMs (Fig. 3), with the largest gaps observed in the intertidal zone (Fig. 2), where land and water surfaces dynamically interact. Copernicus GLO-30 exhibited vertical RMSE values between 1.11 m and 2.54 m, while AW3D30 showed RMSE values between 1.59 m and 2.76 m. For TanDEM-X the range of RMSE values was lower, between 1.19 m and 1.84 m, while Euro-Maps 3D had similar RMSE values for the Outer Banks and Ria Formosa study sites (1.32 m and 1.20 m, respectively). The LE90 values were found to be consistent with those reported by the data providers (Table 1) but also showed variability across sites, ranging from 1.81 m to 3.90 m for Copernicus GLO-30, 2.61 m–4.72 m for AW3D30, 1.82 m–2.73 m for TanDEM-X and remaining relatively consistent for Euro-Maps 3D (2.09 m and 1.92 m). In comparison, TanDEM-X outperformed the other GDEMs with an average RMSE of 1.41 m, a correlation coefficient R of 0.84, an MAE of 1.06 m and an LE90 of 2.29 m (Table 5). For the sites where the higher resolution Euro-Maps 3D data were available (the Outer Banks and the Ria Formosa) TanDEM-X remained the most accurate, followed by Euro-Maps 3D and Copernicus GLO-30 that showed similar accuracy, while AW3D30 presented the highest RMSE, MAE and STD (Table A.1). AW3D30 and Copernicus GLO-30 evidence a consistent tendency to underestimate the elevation of coastal barriers, while TanDEM-X is found to have lower and overall positive bias (Fig. 4). A general underestimation of the dune crest height was observed for all GDEMs.

When averaging alongshore the profiles, the average profile derived from TanDEM-X provided a better representation of the dune crest height, dune face slope, dune leeward slope (Fig. 5) and the overall topographic profile at all locations, with an average correlation coefficient of 0.95 and a RMSE of 0.98 m, while those derived from AW3D30 consistently underestimated the dune top and slope with an average bias of −0.55 m and a RMSE of 1.54 m (Table 5). The profiles derived from Euro-Maps 3D performed similarly to those derived from TanDEM-X, with larger errors on the dune face.

3.2. Evaluation of GBMs' depth accuracy

Similarly to remotely sensed topographic data, GBMs have increased uncertainties in shallow coastal areas compared to the open ocean. This is related to the dynamic nature of the nearshore morphology, and to the fact that GBMs are derived from merging of bathymetric data from different years. From a visual inspection, the GBMs showed larger deviations between each other from 0 m to ~15 m depth, while converging towards a more consistent bathymetric profile with increasing water depth.

The vertical errors of the GBMs vary considerably between the study sites (Fig. 6), with SRTM15+ displaying the largest errors overall, with RMSE values ranging from 1.25 m at Fire Island to 4.87 m at the Outer Banks and a strong bias in the Ria Formosa. Conversely, ETOPO 2022; GEBCO Bathymetric Compilation Group, 2023 were found to have similar and better overall performance compared to SRTM15+ when averaged over the five coastal barriers, with ETOPO 2022 showing higher accuracy (Table 5). The RBMs, such as CUDEM in the USA sites, EMODnet in Europe and the 2023 bathymetric grid of Australia, display high accuracy, with lower RMSE, STD, MAE, Bias and LE90 values compared to the GBMs (Fig. 6, Table A.2 and Table A.3).

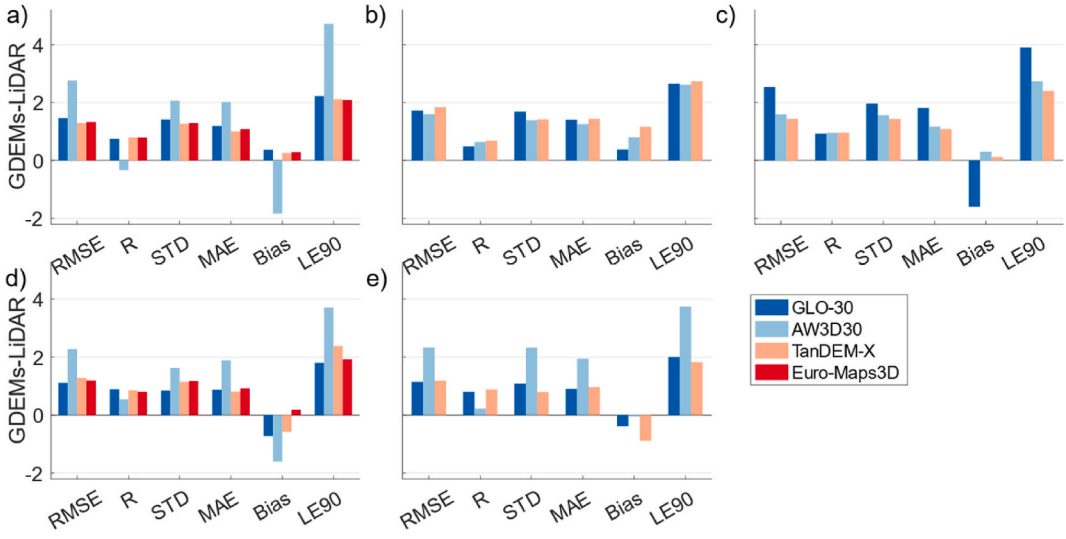

Fig. 3. Error metrics between GDEMs and high-resolution LiDAR-derived DEMs for cross-shore profiles extracted at the Outer Banks in the USA (a), Fire Island in the USA (b), Terschelling in the Netherlands (c), Ria Formosa in southern Portugal (d) and Myalup in Australia (e).

Table 5
Statistical comparison of LiDAR-derived topography and bathymetry against GDEMs/GBMs (from 0 m to ~10 m depth) averaged over all study sites for three cases: a) estimated for all profiles, b) for the average profiles and c) for the merged topo-bathymetric profile obtained from TanDEM-X and ETOPO 2022. Euro-Maps 3D is not included here as data were only available for 2 of the 5 sites.

Dataset			RMSE (m)	R (−)	STD (m)	MAE (m)	Bias (m)	LE90 (m)
All profiles	**Topography**	Copernicus GLO-30	1.60	0.77	1.40	1.24	−0.39	2.52
		AW3D30	2.11	0.40	1.79	1.66	−0.48	3.50
		TanDEM-X	1.41	0.84	1.21	1.06	0.01	2.29
	Bathymetry	SRTM15+V2.0	3.43	0.86	1.80	2.88	1.18	4.78
		GEBCO_2023	2.01	0.98	1.04	1.73	1.58	3.01
		ETOPO 2022	1.81	0.96	1.42	1.27	0.98	2.90
Average profiles	**Topography**	Copernicus GLO-30	1.20	0.91	0.95	1.00	−0.32	1.97
		AW3D30	1.54	0.91	1.14	1.25	−0.55	2.56
		TanDEM-X	0.98	0.95	0.69	0.80	−0.12	1.62
	Bathymetry	SRTM15+V2.0	2.93	0.97	1.31	2.54	2.01	3.75
		GEBCO_2023	1.96	0.99	0.92	1.74	1.64	3.03
		ETOPO 2022	1.83	0.97	1.42	1.32	0.87	2.78
Merged profile	**Topo-bathymetry**	TanDEM-X + ETOPO 2022	0.76	0.99	0.75	0.55	0.01	1.25

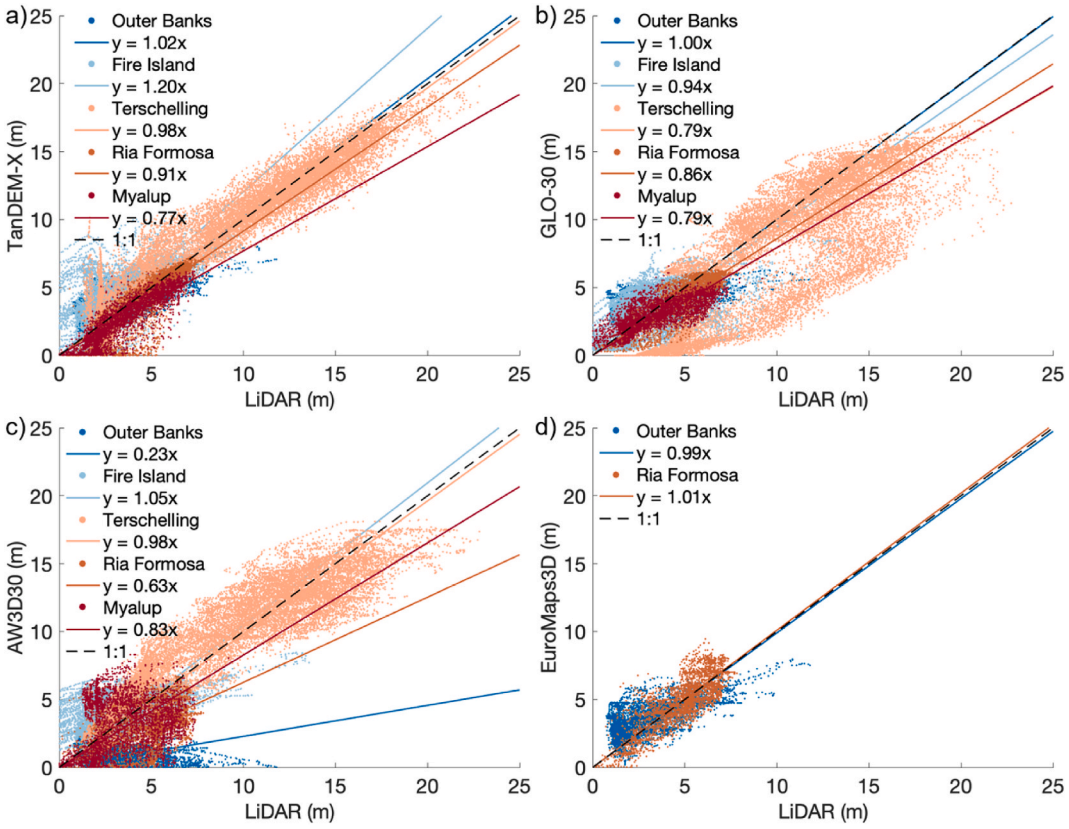

Fig. 4. Comparison between LiDAR-derived elevation and GDEMs for a) TanDEM-X, b) Copernicus GLO-30), c) AW3D30 and d) Euro-Maps 3D. Linear regression lines (forced through the origin) are shown along with their equation for each location. The dashed black line represents a perfect fit.

The regional differences in the accuracy of GBMs were partially explained by the information available in the TID grid for GEBCO Bathymetric Compilation Group, 2023 (which is identical to GEBCO Bathymetric Compilation Group, 2023 TID) and SID for ETOPO 2022 (Fig. A1).

The largest errors in ETOPO 2022 were found at Myalup, where the GEBCO_2022 was used, with 50 % of the data coming from an unknown source. For GEBCO_2023 the largest error was observed in the Outer Banks, where 21 % of the sampled data were based on multiple indirect measurements (satellite-derived gravity data or interpolated bathymetric soundings) that were merged in a relatively small region. In contrast, data from the remaining sites were mostly derived from direct measurements and therefore more accurate. The statistical accuracy of the average bathymetric profiles (Fig. 7) showed a slight improvement compared to the single profiles

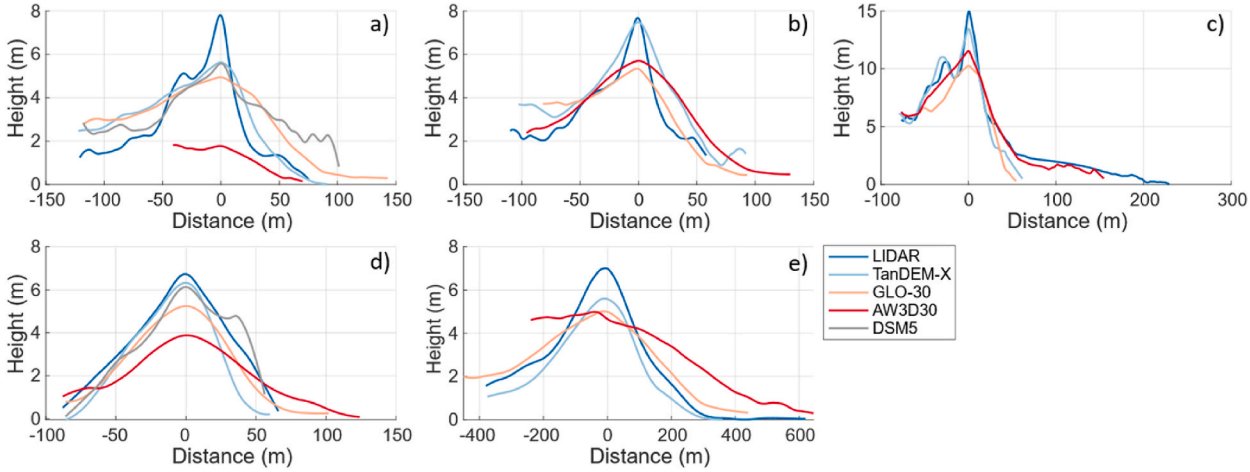

Fig. 5. Averaged topographic profiles aligned at the dune top (x = 0 m) derived from LiDAR and GDEMs at the Outer Banks in the USA (a), Fire Island in the USA (b), Terschelling in the Netherlands (c), Ria Formosa in southern Portugal (d) and Myalup in Australia (e). The ocean is to the right of the profiles.

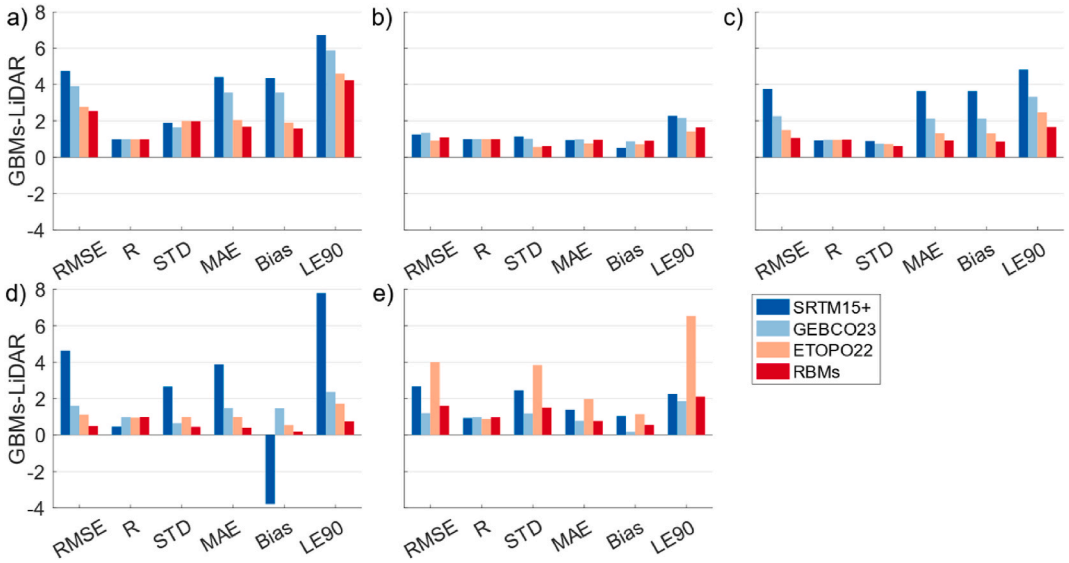

Fig. 6. Error metrics between GBMs and RBMs (CUDEM, EMODnet, 2023 bathymetry of Australia) and high-resolution LiDAR-derived DEMs for cross-shore profiles extracted at the Outer Banks in the USA (a), Fire Island in the USA (b), Terschelling in the Netherlands (c), Ria Formosa in southern Portugal (d) and Myalup in Australia (e).

(Table 5), with ETOPO 2022 showing the highest accuracy across the study sites and SRTM15 v2.0 the lowest.

3.3. Merging of topo-bathymetry and profile elevation accuracy

The merged averaged profiles derived from the GDEMs and GBMs were compared with averaged profiles obtained by merging the LiDAR-derived DEMs with the RBMs. The profile derived from merging TanDEM-X and ETOPO 2022 (Fig. 8 and Table A.4) showed a high performance in terms of statistical fit (low values of MAE, RMSE and bias), although with larger deviations in Myalup. The values estimated for D50 based on profiles derived from merging ETOPO 2022 bathymetry with any GDEM evidence better agreement with the values obtained from the literature (Table A.4), while the profiles derived from merging SRTM15+V2.0 and the GDEMs showed the worst performance (Table A.4).

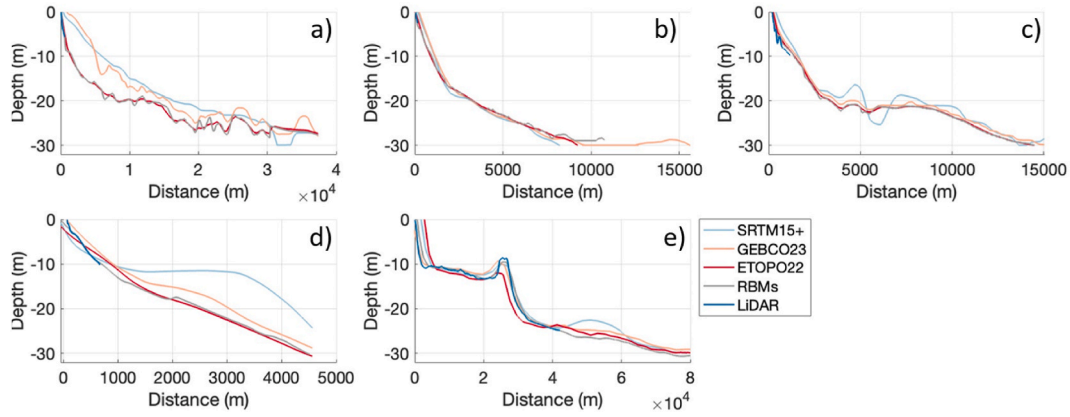

Fig. 7. Averaged bathymetric profiles derived from LiDAR, RBMs and GBMs at the Outer Banks in the USA (a), Fire Island in the USA (b), Terschelling in the Netherlands (c), Ria Formosa in southern Portugal (d) and Myalup in Australia (e).

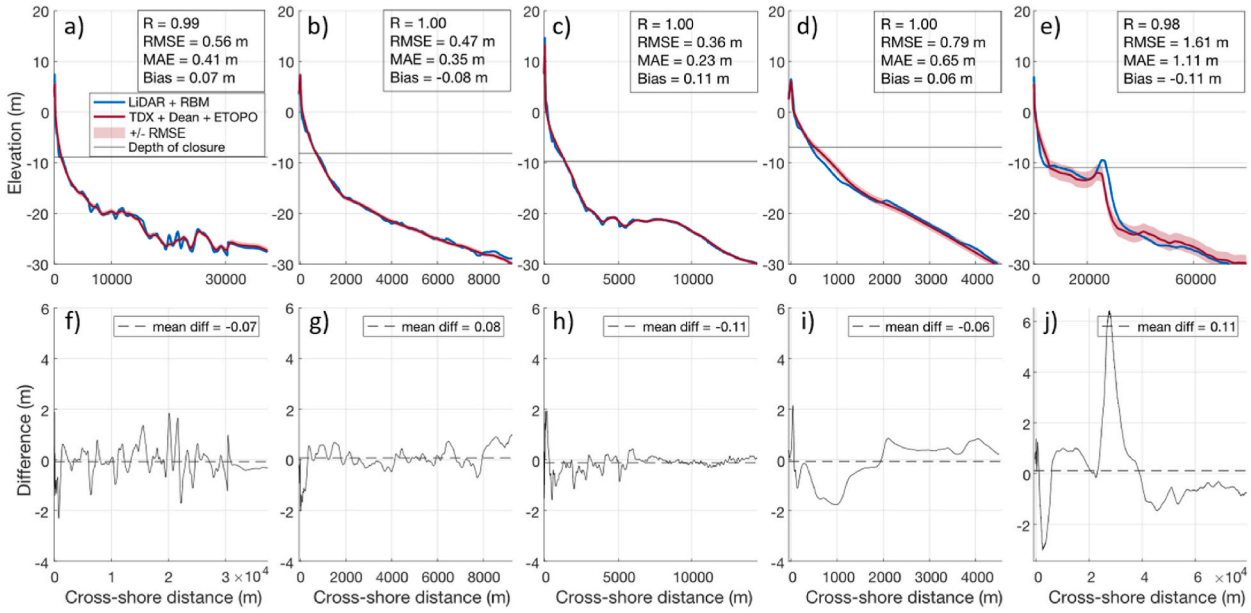

Fig. 8. Top (a to e): Merged topo-bathymetric profiles obtained from LiDAR topography and regional bathymetries (blue line) compared with profiles obtained from merging the equilibrium profile with the TanDEM-X topography and ETOPO 2022 bathymetry (red line) with associated uncertainty of ± RMSE (red envelope). Bottom (f to j): Plot of differences (in meters) between the higher resolution topo-bathymetry derived from merging LiDAR and RBMs and the topo-bathymetry derived from merging TanDEM-X GDEM with ETOPO 2022 GBM. The profiles refer to the coastal barriers at the Outer Banks in the USA (a, f), Fire Island in the USA (b, g), Terschelling in the Netherlands (c, h), Ria Formosa in southern Portugal (d, i) and Myalup in Australia (e, j).

4. Discussion

4.1. Performance of global and regional models

The vertical error assessment of the GDEMs revealed varying levels of accuracy across the study sites. Overall, the RMSE, STD, LE90 and ME determined in the present study are consistent with previous accuracy assessments for the 12 m-resolution TanDEM-X (Chu and Lindenschmidt, 2017; Gesch, 2018; Li et al., 2021; Vassilaki and Stamos, 2020; Wessel et al., 2018; Zhang et al., 2019), AW3D30 (Ding et al., 2023; Gesch, 2018; Li et al., 2022; Takaku et al., 2020; Vassilaki and Stamos, 2020), Copernicus GLO-30 (Hawker et al., 2022; Li et al., 2022) and Euro-Maps 3D (Proietti et al., 2017), with L90 within the range disclosed by each DEM provider (Table 1). However, the errors found in this study were shown to be generally lower than previous assessments. This occurs for several reasons: the evaluation was performed after removing water bodies and spikes in intertidal areas and resampling GDEMs to the LiDAR-derived DEM resolution; the study areas correspond to natural sectors of coastal barriers where buildings and tall vegetation are absent, so

there are fewer artifacts in the GDEMs (Gdulová et al., 2021; Wessel et al., 2018; Zhang et al., 2019); areas with lower slopes are normally associated to higher GDEM accuracy (Li et al., 2022). The largest gaps in the data were found in the intertidal area, where SAR processing is more challenging due to the low backscatter combined with complex coastal morphology, resulting in noisy relief data (Rizzoli et al., 2017; Wendleder et al., 2012). Moreover, cloud cover and homogeneous surfaces such as sand can hinder the processing of optical stereo imagery (Gesch, 2012; Takaku et al., 2020).

According to the statistical evaluation, TanDEM-X outperformed other GDEMs for the characterised coastal barriers (Table 5), in line with previous work by Vassilaki and Stamos (2020) for a range of latitudes, terrain types and land cover classes, and by Li et al. (2021) for different slopes. The performance of Euro-Maps 3D was slightly worse than TanDEM-X, possibly due to the superiority of the SAR sensors over optical sensors (Vassilaki and Stamos, 2020). This was followed by Copernicus GLO-30, which outperformed the other 30 m resolution GDEM, AW3D30, as already verified in Greece (Grigoriadis et al., 2023) and China (Li et al., 2022).

Beyond standard error metrics, when analysing the performance of GDEMs in coastal barriers with a focus on coastal hazards assessments, the dune crest height and beach slope have a critical role in the selection of the best GDEM. An overall underestimation of the dune crest was observed for all GDEMs (Fig. 5), as well as a tendency to overestimate the beach slope, as previously observed for several GDEMs (Almar et al., 2021b; Diaz et al., 2019). Considering this, TanDEM-X was shown to be the GDEM of choice for representing coastal barrier morphology, as it was found to outperform all other GDEMs, including the Euro-Maps 3D commercial dataset. TanDEM-X also provides a better representation of the dune morphology, possibly because Euro-Maps 3D data are stored as integers, which can lead to the flattening of peak values.

Regarding the nearshore bathymetry, which has a fundamental role in wave transformation processes near the coast and, therefore, on coastal flooding (Parodi et al., 2020), storm impact and sea level assessments, or even for the definition of process-based indicators for coastal hazards (Ferreira et al., 2017), there are fewer intercomparisons between GBMs and a higher uncertainty on their overall quality. Moreover, the footprint of altimeter pulses is relatively large, resulting in a limited ability to capture fine-scale details of the seafloor in nearshore areas, while at the same time this dynamic coastal environment is subject to complex morphological features (sandbars, rhythmic forms, channels) and processes (tides, wave action, currents, and sediment transport).

To quantify the uncertainties in the bathymetric data for the selected coastal barriers, three GBMs and three RBMs were evaluated against higher resolution bathymetric data available for areas shallower than −10 m. The GBMs considered here showed lower RMSE, STD and MAE values (Fig. 6) compared to previous assessments (Li et al., 2023; Vrdoljak, 2021). This is likely explained by the smoothing that resulted from the interpolation applied to resample the GBM cell size to that of the LiDAR-derived DEMs, as well as by the fact that in some areas GBMs integrate higher resolution data, as is the case for GEBCO Bathymetric Compilation Group, 2023. The GBMs tend to agree with each other in deeper areas most likely because they are based on the same source for those depths (GEBCO Bathymetric Compilation Group, 2023; NOAA National Centers for Environmental Information, 2022; ETOPO 2022 outperformed all other GBMs across the five locations (Table 5). It was followed by GEBCO Bathymetric Compilation Group, 2023, which had a similar performance, while SRTM15+V2.0 showed the largest errors. This may be due to the fact that GEBCO Bathymetric Compilation Group, 2023 is based on SRTM15+V2.0 and augmented by direct soundings and ETOPO 2022 is based on GEBCO Bathymetric Compilation Group, 2023, also augmented with local higher resolution data. When available, RBMs should be the bathymetric dataset of choice. Otherwise, and considering the frequent updates of GBMs, the latest versions and models should be preferred.

4.2. *Challenges for the topo-bathymetric continuum in poorly surveyed areas*

The coastal topo-bathymetric continuum can be derived from different sensors, with different levels of accuracy and resolution (Li et al., 2023) and presenting different challenges (Eakins and Grothe, 2014). New products have recently been developed to map the intertidal area at higher resolution from space-borne data (Cesbron et al., 2021), including from Pleiades satellite imagery (Almar et al., 2019; Almeida et al., 2019), but also from Sentinel imagery (Almar et al., 2021a; Darmanin et al., 2023; Fitton et al., 2021; Khan et al., 2019), ICESat-2 data (Ma et al., 2023; Xu et al., 2022) and –VENμS (Bergsma et al., 2021). However, only altimeter-derived gravity data from satellites can currently provide global coverage of the ocean floor, although with lower resolution, and therefore most of the published GBMs are still based on this technology. For this reason, the use of GBMs and GDEMs is inevitable for global (e.g. Muis et al., 2020; Parodi et al., 2020; Sepúlveda et al., 2020; Vousdoukas et al., 2020) and regional assessments (e.g. Bove et al., 2020; Gesch, 2009), and they remain a valuable option in remote or poorly surveyed areas where high quality alternatives are absent (Parodi et al., 2020; Vousdoukas et al., 2022). Although beyond the scope of this study, the integration of multiple remote sensing techniques and products can further improve the characterisation of shallow nearshore bathymetry (Ma et al., 2023), yet not on a global scale.

This study complements previous assessments of large-scale remote sensing-based DEM products proposing a new method to improve the application of GDEMs and GBMs in coastal barriers, characterized by the presence of dune morphologies. The methodology was developed by averaging topo-bathymetric DEMs along homogeneous sectors and replacing missing or inaccurate data in the shallow coastal area with an equilibrium nearshore profile. Given the lack of site-specific grain size information in many coastal areas around the world, an indirect method was applied to derive an empirical fitting by forcing it from the mean sea level to the offshore location where the bathymetry reaches the depth of closure, similar to Holman et al. (2014). The depth of closure was estimated using 28 years of wave data from WAVERYS global wave reanalysis, averaged to avoiding tying the analysis to a specific year or event. The depth of closure formulation from Hallermeier (1981) was adopted, which does not account for non-wave forces (such as the tide) but is a suitable approximation to define the limit of the active coastal zone. The equilibrium profile based on Dean (1991) represents a simplification, which does not explicitly account for site-specific variability in hydrodynamics, sediment properties or nearshore bar dynamics. More accurate formulations have been developed to account for the tide (de Villar et al., 2019) and sandbanks (Holman et al., 2014), but these require detailed local data and cannot be generalized to data poor areas. Consequently, applying a single

equilibrium profile in areas with complex nearshore bar systems, rocky outcrops, or strong seasonal changes imposes limitations on the proposed approach because it does not accurately capture short-to-medium-term nearshore morphodynamic changes.

Therefore, the approach proposed in this study represents an improvement given the lack of accurate bathymetric data from the GBMs and an equilibrium profile that represents wave energy dissipation across the surf zone better than a linear slope. Nevertheless, given the impossibility of accounting for dynamic sandbar systems that are relevant for specific events and areas, the merged topo-bathymetric profile is an adequate approximation for engineering to geological scales and idealised simulations.

Furthermore, previous studies have found equilibrium profiles to be a valuable approximation for nearshore bathymetry, for example when pre-storm bathymetric data are lacking (Matheen et al., 2021). The equilibrium profiles obtained using the method described above were compared with equilibrium profiles obtained using actual D50 values found in the literature for the same coastal areas, except for Myalup where the existence of rocky outcrops on part of the nearshore may justify the large differences between GBMs and multibeam data in the nearshore area. Based on the combinations of GDEMs and GBMs tested, the ones with ETOPO 2022 consistently outperformed other GBMs (Table A.4).

The newly developed method proposed in this work involves the merging of multiple barrier profiles, resulting in the transformation of the existing data from global models into a single simplified and representative profile for a given coastal sector (Fig. 8). The comparison of the seamless topo-bathymetric profiles derived from the global models with the LiDAR-derived topo-bathymetries demonstrates that the combination of TanDEM-X GDEM and ETOPO 2022 GBM delivered the best results. This is evident both in terms of statistical comparison to the higher-resolution LiDAR-derived profiles, with an average RMSE of 0.76 m, and in terms of an accurate representation of the dune morphology, with a lower average underestimation of the dune crest by TanDEM-X of only 1.14 m. An overall underestimation of the dune height is observed for all GDEMs (with an average underestimation of 2.68 m for Copernicus GLO-30, 3.25 m for AW3D30 and 6.50 m for Euro-Maps 3D), as well as the absence of a beach berm due to their coarse resolution (Fig. 5). Such underestimation of morphological features that determine the protective role of coastal barriers can lead to an overestimation of the vulnerability for natural coastal barriers in regional to global studies (Vousdoukas et al., 2016, 2018). This can result, for example in the lowering of thresholds that determine the occurrence of storm-induced overwash or inundation (Sallenger, 2000), potentially overestimating the extent and/or magnitude of coastal flooding hazards. The use of the best possible approach (TanDEM-X) is therefore essential in the application of global models for the definition of coastal hazards and risks. Nevertheless, hazard evaluations derived using GDEMs and GBMs could be considered as worst-case estimates of the possible coastal hazards. Moreover, given the overall RMSE found (Fig. 8), the use of the barrier profiles derived from GDEMs and GBMs for coastal flooding assessments due to a sea level rise of less than 1 m is severely limited.

The findings in this study highlight the critical importance of incorporating a range of vertical uncertainties associated with GDEMs, both when considered individually and when used as merged topo-bathymetric profiles. All GBMs showed an overall positive bias (Table 5), as previously demonstrated in the case of SRTM (Bove et al., 2020 and references therein), resulting in a shallower coastal profile and contributing to an inaccurate consideration of the wave energy dissipation by wave models. A shallower nearshore bathymetry also influences the calculation of storm surge and water levels, increasing the uncertainty in the determination of coastal flooding and erosion hazards. The errors in the GDEMs and GBMs were found to be spatially variable and mainly dependent on slope (Diaz et al., 2019; Li et al., 2022), land cover and terrain type (Leon et al., 2014; Li et al., 2021, 2022), and therefore not easily represented by a single dispersion parameter, such as the RMSE (Leon et al., 2014). For this reason, in coastal barriers it is important to consider the overall RMSE of the topo-bathymetric merged profile, but also the bias and underestimation of the dune crest in GDEMs and nearshore slope in GBMs.

An intrinsic limitation of the barrier profiles obtained by the integration of GDEMs and GBMs is related to the fact that these are neither time nor event-specific. The data were collected over several years and seasons (Wendleder et al., 2012), and therefore cannot be used to infer variability over time. Therefore, any storm or climate related changes, or local scale artificial modification of the coast such as beach nourishment or placement of new infrastructure, must be carefully considered based on up-to-date satellite imagery or survey data before employing global models for analysing specific coastal areas. The interpolation, first in the resampling of the GBMs and GDEMs and then in the alongshore averaging, introduces errors for length scales smaller than the resolution of the original data. In addition, potential vertical datum inconsistencies arising from the complexity of vertical datum corrections in coastal areas (Eakins and Grothe, 2014) and artifacts associated by the presence of vegetation may introduce additional vertical errors that add to the uncertainties mentioned above. For these reasons, it is important to explicitly consider the uncertainty resulting from the original datasets, datum conversions, vegetation and the various processing operations, ideally by providing the error range for the final merged profiles. This ensures that these errors are accounted for, particularly for hazard modelling where intertidal inaccuracies can propagate and affect wave transformation, run-up estimation and inundation assessment. In this study, the average RMSE on the final merged profiles obtained from TanDEM-X and ETOPO 2022 ranged from 0.4 to 1.6 m (Table A.4), which includes all the aforementioned uncertainties. Therefore, the profiles must be considered as generalized morphologies that can be easily implemented to identify and prioritize flooding and erosion hotspots or to estimate geoindicators, such as dune elevation, volume and width as proposed by Carapuço et al. (2016) and dune stability factors (Armaroli et al., 2012; Turner et al., 2024). These profiles can also be useful for rapid assessments at large scales (global, national, or regional), or in areas where higher resolution topo-bathymetric data does not exist. The approach proposed in this study is designed for morphologically homogeneous areas along coastal barriers but could be also implemented in sandy coasts fronted by sparsely vegetated dunes. It is important to note that application of equilibrium beach profiles should only be performed for wave-dominated sandy coastlines, therefore excluding mixed sediment coasts, rocky coasts or tide dominated coastal environments. The applicability of the method might also be limited in areas where coastal infrastructure or beach nourishment significantly altered the natural coastal morphology. The main advantage of the presented methodology is that it allows to extract continuous coastal barrier profiles from which profile indicators can be readily extracted as in

Athanasiou et al. (2023). The topo-bathymetric coastal barrier profiles derived in this work, together with their associated errors, offer a valuable, coherent and sufficiently accurate solution for quantifying exposure to coastal hazards at global scales. They can support first order assessments that help to identify and prioritize coastal risk areas that can then be further studied using higher-resolution data.

5. Conclusion

Topo-bathymetric profiles of coastal barriers were developed by merging GDEMs and GBMs with an equilibrium beach profile derived by estimating the averaged depth of closure. The combination of TanDEM-X and ETOPO 2022 performed better in terms of statistical accuracy when compared to high-resolution LiDAR-derived profiles and in terms of morphological characterisation of the coastal barrier, particularly the dune crest height and beach slope. LiDAR-derived DEMs can provide accurate results at the centimetre scale to capture small changes in topo-bathymetry, but have limitations in terms of spatial coverage, cost, and other logistical challenges. However, at global scales the integration of topo-bathymetric profiles proposed here, derived from global open-access remotely sensed datasets, can provide a cost-effective and readily available solution for coastal hazard assessments over large geographical areas, provided their uncertainties are considered. They can be used across wide areas as a preliminary tool for managing coastal zones, contributing to identifying areas potentially vulnerable to coastal flooding, storm-induced erosion, and sea level rise. Ultimately, they can enable the understanding and mitigation of the impacts of natural hazards on society and risk analysis, which detailed local scale assessments can later address.

Ethical statement for remote sensing applications: society and environment

1) This material is the authors' own original work, which has not been previously published elsewhere.
2) The paper is not currently being considered for publication elsewhere.
3) The paper reflects the authors' own research and analysis in a truthful and complete manner.
4) The paper properly credits the meaningful contributions of co-authors and co-researchers.
5) The results are appropriately placed in the context of prior and existing research.
6) All sources used are properly disclosed (correct citation). Literally copying of text must be indicated as such by using quotation marks and giving proper reference.
7) All authors have been personally and actively involved in substantial work leading to the paper, and will take public responsibility for its content.

CRediT authorship contribution statement

Valeria Fanti: Writing – review & editing, Writing – original draft, Visualization, Validation, Software, Methodology, Formal analysis, Conceptualization. **Carlos Loureiro:** Writing – review & editing, Supervision, Methodology, Conceptualization. **Óscar Ferreira:** Writing – review & editing, Supervision, Methodology, Conceptualization.

Declaration of competing interest

The authors declare that they have no known competing financial interests or personal relationships that could have appeared to influence the work reported in this paper.

Acknowledgements

Valeria Fanti is funded through the FCT PhD Research Scholarships program (ref. 2020.07553.BD). This work was supported by the Portuguese Foundation of Science, under the projects LA/P/0069/2020 granted to the Associate Laboratory ARNET, UIDP/00350/2020 granted to CIMA (https://doi.org/10.54499/UIDP/00350/2020), and CEECINST/00052/2021/CP2792/CT0011 granted to Carlos Loureiro (https://doi.org/10.54499/CEECINST/00052/2021/CP2792/CT0011).

The TanDEM-X DEM tiles were provided by the German Aerospace Center (Proposal ID: DEM_HYDR3317). COP-DEM-GLO-30-R and EURO-MAPS 3D DSM products © DLR e.V. (2014–2018) and © Airbus Defence and Space GmbH (2021) provided under COPERNICUS by the European Union and ESA.WAVERYS data were downloaded from the CMEMS Portal (https://resources.marine.copernicus.eu) dataset "GLOBAL_REANALYSIS_WAV_001_032".

Appendix A. Supplementary data

Table A.1
Average GDEM performance statistics. All GDEMs are averaged only for two sites, Outer Banks in the USA and Ria Formosa in Portugal due to the restricted availability of Euro-Maps3D.

GDEM	RMSE (m)	R (−)	STD (m)	MAE (m)	Bias (m)	LE90 (m)
Copernicus GLO-30	1.29	0.82	1.13	1.03	−0.18	2.02
AW3D30	2.52	0.10	1.84	1.95	−1.72	4.21
TanDEM-X	1.29	0.82	1.21	0.91	−0.16	2.25
Euro-Maps3D	1.26	0.79	1.24	1.00	0.24	2.01

Table A.2
Average GBM performance statistics. All GBMs are averaged only for two sites, Outer Banks and Fire Islands in the USA due to the availability of CUDEM data only for the USA.

GBM	RMSE (m)	R (−)	STD (m)	MAE (m)	Bias (m)	LE90 (m)
SRTM15+V2.0	3.00	0.99	1.52	2.68	2.44	4.50
GEBCO_2023	2.63	0.99	1.33	2.27	2.21	4.02
ETOPO 2022	1.84	0.99	1.28	1.40	1.31	3.01
CUDEM	1.81	0.99	1.30	1.32	1.24	2.94

Table A.3
Average GBM performance statistics. All GBMs are averaged only for two sites, Praia de Faro in Portugal and Terschelling in the Netherlands due to the availability of EMODnet data only for the European coast.

GBM	RMSE (m)	R (−)	STD (m)	MAE (m)	Bias (m)	LE90 (m)
SRTM15+V2.0	4.19	0.69	1.77	3.76	−0.07	6.31
GEBCO_2023	1.93	0.96	0.70	1.80	1.80	2.85
ETOPO 2022	1.31	0.95	0.85	1.15	0.92	2.10
EMODnet	0.77	0.97	0.53	0.66	0.52	1.20

Table A.4
Depth of closure (Dc) calculated with wave height and peak period from the entire WAVERYS series ($H_{12h/y}$; $T_{12h/y}$), median grain size (D50) from the literature and statistical results from the comparison of the profiles obtained merging of GDEMs and GBMs and the profile obtained from LiDAR-derived DEMs and RBMs. D50 values in red are out of the acceptable range of fine (0.125–0.25 mm) to medium (0.25–0.5 mm) sand. The colour scale (blue for higher accuracy, red for lower accuracy) of the mean absolute error (MAE) and root mean squared error (RMSE) is based on the highest and lowest values amongst all sites. The colour scale of the bias is based on the highest and lowest absolute values

Location	Depth of closure	D50 literature	GDEM	GBM	D50 (mm)	R (-)	MAE (m)	RMSE (m)	Bias (m)
Outer Banks, USA	$H_{12h/y}$ = 4.30 m $T_{12h/y}$ = 12.04 s Dc = -8.92 m	D50 = 0.2-0.3 mm (CSE, 2015; Grasso et al., 2009; Safak et al., 2017; Splinter et al., 2014)	TanDEM-X	GEBCO 2023	0.06	0.97	2.99	3.58	2.82
				ETOPO 2022	0.18	0.99	0.41	0.56	0.07
				SRTM15+V2.0	0.05	0.94	3.83	4.59	3.28
			Copernicus GLO-30	GEBCO 2023	0.06	0.97	3.04	3.66	2.87
				ETOPO 2022	0.20	0.99	0.42	0.59	0.08
				SRTM15+V2.0	0.06	0.94	3.77	4.47	3.21
			AW3D30	GEBCO 2023	0.06	0.97	2.99	3.59	2.82
				ETOPO 2022	0.18	0.99	0.41	0.57	0.07
				SRTM15+V2.0	0.05	0.94	3.84	4.60	3.28
Fire Island, USA	$H_{12h/y}$ = 4.07 m $T_{12h/y}$ = 10.18 s Dc = -8.17 m	D50 = 0.2-0.4 mm (Kana et al., 2011)	TanDEM-X	GEBCO 2023	0.22	1.00	0.75	0.93	-0.06
				ETOPO 2022	0.33	1.00	0.35	0.47	-0.08
				SRTM15+V2.0	0.22	1.00	0.90	1.07	-0.29
			Copernicus GLO-30	GEBCO 2023	0.20	1.00	0.75	0.94	-0.07
				ETOPO 2022	0.30	1.00	0.34	0.45	-0.09
				SRTM15+V2.0	0.21	1.00	0.88	1.05	-0.33
			AW3D30	GEBCO 2023	0.22	1.00	0.76	0.96	-0.05
				ETOPO 2022	0.35	1.00	0.36	0.51	-0.07
				SRTM15+V2.0	0.22	1.00	0.91	1.10	-0.28
Terschelling, Netherlands	$H_{12h/y}$ = 5.03 m $T_{12h/y}$ = 10.13 s Dc = -9.74 m	D50 = 0.18-0.21 mm (Athanasiou et al., 2021; Pilarczyk et al., 1989)	TanDEM-X	GEBCO 2023	0.17	1.00	0.83	0.89	0.78
				ETOPO 2022	0.18	1.00	0.23	0.36	0.11
				SRTM15+V2.0	0.16	0.98	1.65	1.93	1.15
			Copernicus GLO-30	GEBCO 2023	0.16	1.00	0.84	0.91	0.78
				ETOPO 2022	0.18	1.00	0.22	0.39	0.08
				SRTM15+V2.0	0.16	0.97	1.64	1.94	1.12
			AW3D30	GEBCO 2023	0.18	1.00	0.84	0.91	0.83
				ETOPO 2022	0.20	1.00	0.23	0.37	0.15
				SRTM15+V2.0	0.17	0.98	1.66	1.95	1.19
Ria Formosa, Portugal	$H_{12h/y}$ = 3.38 m $T_{12h/y}$ = 10.10 s Dc = -6.93 m	D50 = 0.5 mm (Kombiadou et al., 2021; Poelhekke et al., 2016)	TanDEM-X	GEBCO 2023	0.25	1.00	1.98	2.08	1.93
				ETOPO 2022	0.33	1.00	0.65	0.79	0.06
				SRTM15+V2.0	0.53	0.92	6.15	7.19	5.97
				GEBCO 2023	0.27	1.00	2.01	2.09	1.97
			Copernicus GLO-30	ETOPO 2022	0.36	1.00	0.67	0.80	0.09
				SRTM15+V2.0	0.94	0.92	6.16	7.19	5.97
			AW3D30	GEBCO 2023	0.31	1.00	2.06	2.13	1.98
				ETOPO 2022	0.43	1.00	0.72	0.87	0.10
				SRTM15+V2.0	1.27	0.93	6.18	7.18	5.96
Myalup, Australia	$H_{12h/y}$ = 5.71 m $T_{12h/y}$ = 14.10 s Dc = -11.87 m	D50 = 0.22 mm (Short, 2022)	TanDEM-X	GEBCO 2023	0.06	0.99	1.15	1.33	0.89
				ETOPO 2022	0.06	0.98	1.11	1.61	-0.11
				SRTM15+V2.0	0.06	0.99	1.24	1.68	1.05
			Copernicus GLO-30	GEBCO 2023	0.06	0.99	1.17	1.37	0.93
				ETOPO 2022	0.07	0.98	1.08	1.58	-0.13
				SRTM15+V2.0	0.06	0.99	1.26	1.71	1.09
			AW3D30	GEBCO 2023	0.06	0.99	1.20	1.41	0.97
				ETOPO 2022	0.07	0.98	1.11	1.61	-0.10
				SRTM15+V2.0	0.06	0.99	1.29	1.74	1.12

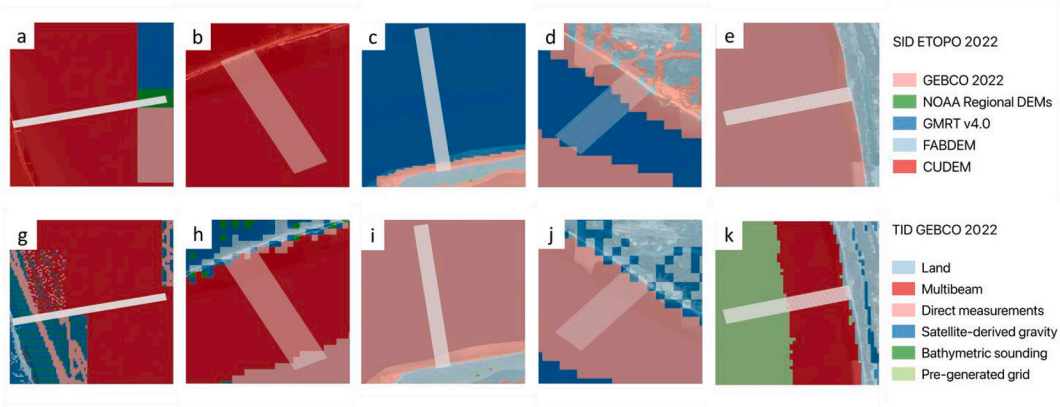

Fig. A.1. Source ID grids from ETOPO 2022 (a to e) and Type Identifier grids from GEBCO Bathymetric Compilation Group, 2023 (f to j) for the Outer Banks in the USA (a-f), Fire Island in the USA (b-g), Terschelling in the Netherlands (c-h), Ria Formosa in Portugal (d-i), Myalup in Australia (e-j). For each coastal barrier the extracted cross-shore profiles until 30 m depth are represented in white.

Data availability

Data will be made available on request.

References

Almar, R., Bergsma, E.W.J., Maisongrande, P., de Almeida, L.P.M., 2019. Wave-derived coastal bathymetry from satellite video imagery: a showcase with Pleiades persistent mode. Remote Sens. Environ. 231, 111263. https://doi.org/10.1016/j.rse.2019.111263.

Almar, R., Bergsma, E.W.J., Thoumyre, G., Baba, M.W., Cesbron, G., Daly, C., Garlan, T., Lifermann, A., 2021a. Global satellite-based coastal bathymetry from waves. Remote Sens. 13, 1–13. https://doi.org/10.3390/rs13224628.

Almar, R., Ranasinghe, R., Bergsma, E.W.J., Diaz, H., Melet, A., Papa, F., Vousdoukas, M., Athanasiou, P., Dada, O., Almeida, L.P.M., Kestenare, E., 2021b. A global analysis of extreme coastal water levels with implications for potential coastal overtopping. Nat. Commun. 12, 1–9. https://doi.org/10.1038/s41467-021-24008-9.

Almeida, L.P.M., Almar, R., Bergsma, E.W.J., Berthier, E., Baptista, P., Garel, E., Dada, O.A., Alves, B., 2019. Deriving high spatial-resolution coastal topography from sub-meter satellite stereo imagery. Remote Sens. 11, 590. https://doi.org/10.3390/rs11050590.

Amante, C.J., Love, M., Carignan, K., Sutherland, M.G., MacFerrin, M., Lim, E., 2023. Continuously updated digital elevation models (CUDEMs) to support coastal inundation modeling. Remote Sens. 15, 1702. https://doi.org/10.3390/rs15061702.

Aragonés, L., Serra, J.C., Villacampa, Y., Saval, J.M., Tinoco, H., 2016. New methodology for describing the equilibrium beach profile applied to the Valencia's beaches. Geomorphology 259, 1–11. https://doi.org/10.1016/j.geomorph.2015.06.049.

Archer, L., Neal, J.C., Bates, P.D., House, R.J., 2018. Comparing TanDEM-X data with frequently-used DEMs for flood inundation modeling. Water Resour. Res. 54, 10–205. https://doi.org/10.1029/2018WR023688.

Armaroli, C., Ciavola, P., Perini, L., Calabrese, L., Lorito, S., Valentini, A., Masina, M., 2012. Critical storm thresholds for significant morphological changes and damage along the Emilia-Romagna coastline, Italy. Geomorphology 143–144, 34–51. https://doi.org/10.1016/j.geomorph.2011.09.006.

Ashphaq, M., Srivastava, P.K., Mitra, D., 2021. Review of near-shore satellite derived bathymetry: classification and account of five decades of coastal bathymetry research. J. Ocean Eng. Sci. 6, 340–359. https://doi.org/10.1016/j.joes.2021.02.006.

Athanasiou, P., van Dongeren, A.R., Giardino, A., Vousdoukas, M.I., Antolínez, J.A.Á., Ranasinghe, R., 2021. A clustering approach for predicting dune morphodynamic response to storms using typological coastal profiles: a case study at the Dutch coast. Front. Mar. Sci. 8, 1–20. https://doi.org/10.3389/fmars.2021.747754.

Athanasiou, P., van Dongeren, A.R., Pronk, M., Giardino, A., Vousdoukas, M.I., Ranasinghe, R., 2023. Preprint Global Coastal Characteristics (GCC): a global dataset of geophysical, hydrodynamic and socioeconomic coastal indicators. Earth Syst. Sci. Data Discuss. (submitted for publication).

Beaman, R., 2023. AusBathyTopo 250m (Australia) 2023 - a high-resolution depth model for Australia. https://dx.doi.org/10.26186/148758.

Bergsma, E.W.J., Almar, R., Rolland, A., Binet, R., Brodie, K.L., Bak, A.S., 2021. Coastal morphology from space: a showcase of monitoring the topography-bathymetry continuum. Remote Sens. Environ. 261, 112469. https://doi.org/10.1016/j.rse.2021.112469.

Bishop-Taylor, R., Sagar, S., Lymburner, L., Beaman, R.J., 2019. Between the tides: modelling the elevation of Australia's exposed intertidal zone at continental scale. Estuar. Coast Shelf Sci. 223, 115–128. https://doi.org/10.1016/j.ecss.2019.03.006.

Bove, G., Becker, A., Sweeney, B., Vousdoukas, M.I., Kulp, S., 2020. A method for regional estimation of climate change exposure of coastal infrastructure: case of USVI and the influence of digital elevation models on assessments. Sci. Total Environ. 710, 136162. https://doi.org/10.1016/j.scitotenv.2019.136162.

Bruun, P., 1954. Coast Erosion and the Development of Beach Profiles. US Beach Erosion Board, Washington DC.

Caballero, I., Stumpf, R.P., 2019. Retrieval of nearshore bathymetry from Sentinel-2A and 2B satellites in South Florida coastal waters. Estuar. Coast Shelf Sci. 226, 106277. https://doi.org/10.1016/j.ecss.2019.106277.

Carapuço, M.M., Taborda, R., Silveira, T.M., Psuty, N.P., Andrade, C., Freitas, M.C., 2016. Coastal geoindicators: towards the establishment of a common framework for sandy coastal environments. Earth Sci. Rev. 154, 183–190. https://doi.org/10.1016/j.earscirev.2016.01.002.

Cesbron, G., Melet, A., Almar, R., Lifermann, A., Tullot, D., Crosnier, L., 2021. Pan-European Satellite-derived coastal bathymetry—review, user needs and future services. Front. Mar. Sci. 8, 1–15. https://doi.org/10.3389/fmars.2021.740830.

Chu, T., Lindenschmidt, K.E., 2017. Comparison and validation of digital elevation models derived from InSAR for a flat inland delta in the high latitudes of Northern Canada. Can. J. Rem. Sens. 43, 109–123. https://doi.org/10.1080/07038992.2017.1286936.

Collins, J., Riegler, G., Schrader, H., Tinz, M., 2015. Applying terrain and hydrological editing to TanDEM-X data to create a consumer-ready WorldDEM product. Int. Arch. Photogram. Rem. Sens. Spatial Inf. Sci. 40, 1149–1154. https://doi.org/10.5194/isprsarchives-XL-7-W3-1149-2015.

Cooper, J.A.G., Green, A.N., Loureiro, C., 2018. Geological constraints on mesoscale coastal barrier behaviour. Global Planet. Change 168, 15–34. https://doi.org/10.1016/j.gloplacha.2018.06.006.

Crippen, R., Buckley, S., Agram, P., Belz, E., Gurrola, E., Hensley, S., Kobrick, M., Lavalle, M., Martin, J., Neumann, M., Nguyen, Q., Rosen, P., Shimada, J., Simard, M., Tung, W., 2016. NASADEM global elevation model: methods and progress. Int. Arch. Photogram. Rem. Sens. Spatial Inf. Sci. 41, 125–128. https://doi.org/10.5194/isprsarchives-XLI-B4-125-2016.

CSE, 2015. Appendix C - GEOTECHNICAL DATA REPORT beach restoration to protect NC highway 12 at buxton. Dare County. North Carolina.

Cyrille, P., Gael, B., Anthony, S., 2021. Global Estimated Surfaces of Lowest Astronomical Tide (LAT) and Mean Sea Level (MSL). SEANOE. https://doi.org/10.17882/85408 [WWW Document].

Darmanin, G., Gauci, A., Deidun, A., Galone, L., D'Amico, S., 2023. Satellite-derived bathymetry for selected shallow Maltese coastal zones. Appl. Sci. 13, 5238. https://doi.org/10.3390/app13095238.

de Villar, A.C., Gómez-Pina, G., Muñoz-Pérez, J.J., Contreras, F., López-García, P., Ruiz-Ortiz, V., 2019. New design parameters for biparabolic beach profiles (SW Cadiz, Spain). Rev. la Constr. 18, 432–444. https://doi.org/10.7764/RDLC.18.3.432.

Dean, R.G., 1991. Equilibrium beach profiles: characteristics and applications. J. Coast Res. 7, 53–84.

Dean, R.G., 2003. Beach nourishment: theory and practice. In: World Scientific, vol. 18. https://doi.org/10.1142/2160.

Diaz, H., Almar, R., Bergsma, E.W.J., Leger, F., 2019. On the use of satellite-based Digital Elevation Models to determine coastal topography. Int. Geosci. Remote Sens. Symp, pp. 8201–8204. https://doi.org/10.1109/IGARSS.2019.8899189.

Ding, H., Liu, J., Yang, S., Luo, J., Liu, Y., Jiang, S., Fu, Y., Liang, X., Na, J., 2023. Performance assessment of global open-access digital elevation models in China mainland coastal region. Earth Surf. Process. Landf. 48, 2133–2140. https://doi.org/10.1002/esp.5677.

Direcção-Geral do Território, 2011. Modelo Digital do Terreno das Zonas Costeiras de Portugal Continental com resolução de 2 m (600 m mar , 400 m terra) - LiDAR. Lisboa.

Eakins, B.W., Grothe, P.R., 2014. Challenges in building coastal digital elevation models. J. Coast Res. 30, 942–953. https://doi.org/10.2112/JCOASTRES-D-13-00192.1.

El-Quilish, M., El-Ashquer, M., Dawod, G., El-Fiky, G., 2018. Development and accuracy assessment of high-resolution digital elevation model using GIS approaches for the Nile Delta Region, Egypt. Am. J. Geogr. Inf. Syst. 7, 107–117. https://doi.org/10.5923/j.ajgis.20180704.02.

Fahrland, E., Jacob, P., Schrader, H., Kahabka, H., 2020. Copernicus Digital Elevation Model Product Handbook. Airbus Defence and Space—Intelligence, Potsdam. Germany.

Fandé, M.B., Lira, C.P., Penha-Lopes, G., 2022. Using TanDEM-X global DEM to map coastal flooding exposure under sea-level rise : application to Guinea-bissau. Int. J. Geo-Inform. 11, 1–20. https://doi.org/10.3390/ijgi11040225.

Fanti, V., Ferreira, Ó., Kümmerer, V., Loureiro, C., 2023. Improved estimates of extreme wave conditions in coastal areas from calibrated global reanalyses. Commun. Earth Environ. 4, 151. https://doi.org/10.1038/s43247-023-00819-0.

Farr, T.G., Rosen, P.A., Caro, E., Crippen, R., Duren, R., Hensley, S., Kobrick, M., Paller, M., Rodriguez, E., Roth, L., Seal, D., 2007. The shuttle radar topography mission. Rev. Geophys. 45, 1–33. https://doi.org/10.1007/3-540-44818-7_11.

Ferreira, Ó., Plomaritis, T.A., Costas, S., 2017. Process-based indicators to assess storm induced coastal hazards. Earth Sci. Rev. 173, 159–167. https://doi.org/10.1016/j.earscirev.2017.07.010.

Fitton, J.M., Rennie, A.F., Hansom, J.D., Muir, F.M.E., 2021. Remotely sensed mapping of the intertidal zone: a Sentinel-2 and Google Earth Engine methodology. Remote Sens. Appl. Soc. Environ. 22, 100499. https://doi.org/10.1016/j.rsase.2021.100499.

Gdulová, K., Marešová, J., Barták, V., Szostak, M., Červenka, J., Moudrý, V., 2021. Use of tandem-x and srtm-c data for detection of deforestation caused by bark beetle in central european mountains. Remote Sens. 13, 1–17. https://doi.org/10.3390/rs13153042.

GEBCO Bathymetric Compilation Group, 2023. The GEBCO_2023 Grid. https://doi.org/10.5285/f98b053b-0cbc-6c23-e053-6c86abc0af7b.

Gesch, D.B., 2018. Best practices for elevation-based assessments of sea-level rise and coastal flooding exposure. Front. Earth Sci. 6. https://doi.org/10.3389/feart.2018.00230.

Gesch, D.B., 2012. Global digital elevation model development from satellite remote-sensing data. In: Advances in Mapping from Remote Sensor Imagery: Techniques and Applications, pp. 92–109. https://doi.org/10.1201/b13770-5.

Gesch, D.B., 2009. Analysis of lidar elevation data for improved identification and delineation of lands vulnerable to sea-level rise. J. Coast Res. 49–58. https://doi.org/10.2112/SI53-006.1, 2009.

Gharagozlou, A., Dietrich, J.C., Karanci, A., Luettich, R.A., Overton, M.F., 2020. Storm-driven erosion and inundation of barrier islands from dune-to region-scales. Coast. Eng. 158, 103674. https://doi.org/10.1016/j.coastaleng.2020.103674.

González, C., Bachmann, M., Bueso-Bello, J.L., Rizzoli, P., Zink, M., 2020. A fully automatic algorithm for editing the TanDEM-X global DEM. Remote Sens. 12, 1–23. https://doi.org/10.3390/rs12233961.

Grasso, F., Michallet, H., Barthélemy, E., Certain, R., 2009. Physical modeling of intermediate cross-shore beach morphology: transients and equilibrium states. J. Geophys. Res. Ocean. 114, 1–15. https://doi.org/10.1029/2009JC005308.

Grigoriadis, V.N., Andritsanos, V.D., Natsiopoulos, D.A., 2023. Validation of recent DSM/DEM/DBMs in test areas in Greece using spirit leveling, GNSS, gravity and echo sounding measurements. ISPRS Int. J. GeoInf. 12. https://doi.org/10.3390/ijgi12030099.

Hallermeier, R., 1981. A profile zonation for seasonal sand beaches from wave climate. Coast. Eng. 4, 253–277.

Hawker, L., Bates, P., Neal, J., Rougier, J., 2018a. Perspectives on digital elevation model (DEM) simulation for flood modeling in the absence of a high-accuracy open access global DEM. Front. Earth Sci. 6, 1–9. https://doi.org/10.3389/feart.2018.00233.

Hawker, L., Rougier, J., Neal, J., Bates, P., Archer, L., Yamazaki, D., 2018b. Implications of simulating global digital elevation models for flood inundation studies. Water Resour. Res. 54, 7910–7928. https://doi.org/10.1029/2018WR023279.

Hawker, L., Uhe, P., Paulo, L., Sosa, J., Savage, J., Sampson, C., Neal, J., 2022. A 30 m global map of elevation with forests and buildings removed. Environ. Res. Lett. 17. https://doi.org/10.1088/1748-9326/ac4d4f.

Her, Y., Heatwole, C.D., Kang, M.S., 2015. Interpolating SRTM elevation data to higher resolution to improve hydrologic analysis. J. Am. Water Resour. Assoc. 51, 1072–1087. https://doi.org/10.1111/jawr.12287.

Holman, R.A., Lalejini, D.M., Edwards, K., Veeramony, J., 2014. A parametric model for barred equilibrium beach profiles. Coast. Eng. 90, 85–94. https://doi.org/10.1016/j.coastaleng.2014.03.005.

IHO, 2023. Status of Hydrographic Surveying and Charting Worldwide.

IHO, 2022. Standards for Hydrographic Surveys.

IPCC, 2022. Climate Change 2022: Impacts, Adaptation and Vulnerability. Contribution of Working Group II to the Sixth Assessment Report of the Intergovernmental Panel on Climate Change. Cambridge University Press, Cambridge, UK and New York, NY, USA, Cambridge, UK and New York, NY, USA. https://doi.org/10.1017/9781009325844.

Irish, J.L., Frey, A.E., Rosati, J.D., Olivera, F., Dunkin, L.M., Kaihatu, J.M., Ferreira, C.M., Edge, B.L., 2010. Potential implications of global warming and barrier island degradation on future hurricane inundation, property damages, and population impacted. Ocean Coast Manag. 53, 645–657. https://doi.org/10.1016/j.ocecoaman.2010.08.001.

Kana, T.W., Rosati, J.D., Traynum, S.B., 2011. Lack of evidence for onshore sediment transport from deep water at decadal time scales: Fire Island, New York. J. Coast Res. 59, 61–75. https://doi.org/10.2307/29783103.

Khan, M.J.U., Ansary, M.N., Durand, F., Testut, L., Ishaque, M., Calmant, S., Krien, Y., Saifu, A.K.M., Papa, F., 2019. High-resolution intertidal topography from Sentinel-2 multi-spectral imagery: synergy between remote sensing and numerical modeling. Remote Sens. 11, 1–20. https://doi.org/10.3390/rs11242888.

Kidner, D.B., 2003. Higher-order interpolation of regular grid digital elevation models. Int. J. Rem. Sens. 24, 2981–2987. https://doi.org/10.1080/0143116031000086835.

Kombiadou, K., Costas, S., Roelvink, D., 2021. Simulating destructive and constructive morphodynamic processes in steep beaches. J. Mar. Sci. Eng. 9, 1–19. https://doi.org/10.3390/jmse9010086.
Kulp, S., Strauss, B.H., 2019. New elevation data triple estimates of global vulnerability to sea-level rise and coastal flooding. Nat. Commun. 10, 1–12. https://doi.org/10.1038/s41467-019-12808-z.
Kulp, S., Strauss, B.H., 2016. Global DEM errors underpredict coastal vulnerability to sea level rise and flooding. Front. Earth Sci. 4, 1–8. https://doi.org/10.3389/feart.2016.00036.
Law-Chune, S., Aouf, L., Dalphinet, A., Levier, B., Drillet, Y., Drevillon, M., 2021. WAVERYS: a CMEMS global wave reanalysis during the altimetry period. Ocean Dyn. 71, 357–378. https://doi.org/10.1007/s10236-020-01433-w.
Leon, J.X., Heuvelink, G.B.M., Phinn, S.R., 2014. Incorporating DEM uncertainty in coastal inundation mapping. PLoS One 9, e108727. https://doi.org/10.1371/journal.pone.0108727.
Li, H., Zhao, J., Yan, B., Yue, L., Wang, L., 2022. Global DEMs vary from one to another: an evaluation of newly released Copernicus, NASA and AW3D30 DEM on selected terrains of China using ICESat-2 altimetry data. Int. J. Digit. Earth 15, 1149–1168. https://doi.org/10.1080/17538947.2022.2094002.
Li, P., Li, Z., Dai, K., Al-Husseinawi, Y., Feng, W., Wang, H., 2021. Reconstruction and evaluation of DEMs from bistatic TanDEM-X SAR in mountainous and coastal areas of China. IEEE J. Sel. Top. Appl. Earth Obs. Rem. Sens. 14, 5152–5170. https://doi.org/10.1109/JSTARS.2021.3073782.
Li, Z., Peng, Z., Zhang, Z., Chu, Y., Xu, C., Yao, S., García-Fernández, Á.F., Zhu, X., Yue, Y., Levers, A., Zhang, J., Ma, J., 2023. Exploring modern bathymetry: a comprehensive review of data acquisition devices, model accuracy, and interpolation techniques for enhanced underwater mapping. Front. Mar. Sci. 10, 1–22. https://doi.org/10.3389/fmars.2023.1178845.
Ma, Y., Wang, L., Xu, N., Zhang, S., Hua Wang, X., Li, S., 2023. Estimating coastal slope of sandy beach from ICESat-2: a case study in Texas. Environ. Res. Lett. 18. https://doi.org/10.1088/1748-9326/acc87d.
Marešová, J., Gdulová, K., Pracná, P., Moravec, D., Gábor, L., Prošek, J., Barták, V., Moudrý, V., 2021. Applicability of data acquisition characteristics to the identification of local artefacts in global digital elevation models: comparison of the Copernicus and TanDEM-X DEMs. Remote Sens. 13, 1–18. https://doi.org/10.3390/rs13193931.
Mason, D.C., Garcia-Pintado, J., Cloke, H.L., Dance, S.L., 2015. The potential of flood forecasting using a variable-resolution global digital terrain model and flood extents from synthetic aperture radar images. Front. Earth Sci. 3, 1–14. https://doi.org/10.3389/feart.2015.00043.
Mason, D.C., Trigg, M., Garcia-Pintado, J., Cloke, H.L., Neal, J.C., Bates, P.D., 2016. Improving the TanDEM-X digital elevation model for flood modelling using flood extents from synthetic aperture radar images. Remote Sens. Environ. 173, 15–28. https://doi.org/10.1016/j.rse.2015.11.018.
Matheen, N., Harley, M.D., Turner, I.L., Splinter, K.D., Simmons, J.A., Thran, M.C., 2021. Bathymetric data requirements for operational coastal erosion forecasting using xbeach. J. Mar. Sci. Eng. 9. https://doi.org/10.3390/jmse9101053.
Mayer, L., Jakobsson, M., Allen, G., Dorschel, B., Falconer, R., Ferrini, V., Lamarche, G., Snaith, H., Weatherall, P., 2018. The Nippon Foundation-GEBCO seabed 2030 project: the quest to see the world's oceans completely mapped by 2030. Geosci. 8. https://doi.org/10.3390/geosciences8020063.
McBride, R.A., Anderson, J.B., Buynevich, I.V., Byrnes, M.R., Cleary, W., Fenster, M.S., FitzGerald, D.M., Hapke, C.J., Harris, M.S., Hein, C.J., Johnson, C.L., Klein, A. H.F., Liu, B., De Menezes, J.T., Mulhern, J.S., Oliver, T.S.N., Pejrup, M., Riggs, S.R., Roberts, H.H., Rodriguez, A.B., Seminack, C.T., Short, A.D., Stone, G.W., Tamura, T., Wallace, D.J., Wang, P., 2022. Morphodynamics of modern and ancient barrier systems: an updated and expanded synthesis. Treatise on Geomorphology. Elsevier. https://doi.org/10.1016/B978-0-12-818234-5.00153-X.
Melet, A., Teatini, P., Le Cozannet, G., Jamet, C., Conversi, A., Benveniste, J., Almar, R., 2020. Earth observations for monitoring marine coastal hazards and their drivers. Surv. Geophys. https://doi.org/10.1007/s10712-020-09594-5. Springer Netherlands.
Muis, S., Apecechea, M.I., Dullaart, J., de Lima Rego, J., Madsen, K.S., Su, J., Yan, K., Verlaan, M., 2020. A high-resolution global dataset of extreme sea levels, tides, and storm surges, including future projections. Front. Mar. Sci. 7, 1–15. https://doi.org/10.3389/fmars.2020.00263.
Neumann, B., Vafeidis, A.T., Zimmermann, J., Nicholls, R.J., 2015. Future coastal population growth and exposure to sea-level rise and coastal flooding - a global assessment. PLoS One 10. https://doi.org/10.1371/journal.pone.0118571.
Nguyen, T.T.X., Bonetti, J., Rogers, K., Woodroffe, C.D., 2016. Indicator-based assessment of climate-change impacts on coasts : a review of concepts , methodological approaches and vulnerability indices. Ocean Coast Manag. 123, 18–43. https://doi.org/10.1016/j.ocecoaman.2015.11.022.
NOAA National Centers for Environmental Information, 2022. ETOPO 2022 15 arc-second global relief model. https://doi.org/10.25921/fd45-gt74.
Pacheco, A., Horta, J., Loureiro, C., Ferreira, Ó., 2015. Retrieval of nearshore bathymetry from Landsat 8 images: a tool for coastal monitoring in shallow waters. Remote Sens. Environ. 159, 102–116. https://doi.org/10.1016/j.rse.2014.12.004.
Parodi, M.U., Giardino, A., Van Dongeren, A.R., Pearson, S.G., Bricker, J.D., Reniers, A.J.H.M., 2020. Uncertainties in coastal flood risk assessments in small island developing states. Nat. Hazards Earth Syst. Sci. 20, 2397–2414. https://doi.org/10.5194/nhess-20-2397-2020.
Pdok, L., 2017. Besteksvoorwaarden Inwinning Landsdekkende Dataset AHN2014–2019: Technical Report 3.0 Final.
Pilarczyk, K.W., Verhagen, H.J., Roelse, P., Adriaanse, L., Consemulder, J., 1989. Handboek Zandsuppleties, Uitgever Waltman.
Pleskachevsky, A., Lehner, S., Heege, T., Mott, C., 2011. Synergy and fusion of optical and synthetic aperture radar satellite data for underwater topography estimation in coastal areas. Ocean Dyn. 61, 2099–2120. https://doi.org/10.1007/s10236-011-0460-1.
Poelhekke, L., Jäger, W.S., van Dongeren, A.R., Plomaritis, T.A., McCall, R.T., Ferreira, Ó., 2016. Predicting coastal hazards for sandy coasts with a Bayesian Network. Coast. Eng. 118, 21–34. https://doi.org/10.1016/j.coastaleng.2016.08.011.
Proietti, S., Lorenzon, F., Uttenthaler, A., Klaus, A., Probeck, M., 2017. Overview of Global DEM: Assessment of the Current Global DEMs and Requirements for an Updated Global DEM.
Rizzoli, P., Martone, M., Gonzalez, C., Wecklich, C., Borla Tridon, D., Bräutigam, B., Bachmann, M., Schulze, D., Fritz, T., Huber, M., Wessel, B., Krieger, G., Zink, M., Moreira, A., 2017. Generation and performance assessment of the global TanDEM-X digital elevation model. ISPRS J. Photogrammetry Remote Sens. 132, 119–139. https://doi.org/10.1016/j.isprsjprs.2017.08.008.
Safak, I., List, J.H., Warner, J.C., Kumar, N., 2017. Observations and 3D hydrodynamics-based modeling of decadal-scale shoreline change along the Outer Banks, North Carolina. Coast. Eng. 120, 78–92. https://doi.org/10.1016/j.coastaleng.2016.11.014.
Salameh, E., Frappart, F., Almar, R., Baptista, P., Heygster, G., Lubac, B., Raucoules, D., Almeida, L.P.M., Bergsma, E.W.J., Capo, S., De Michele, M.D., Idier, D., Li, Z., Marieu, V., Poupardin, A., Silva, P.A., Turki, I., Laignel, B., 2019. Monitoring beach topography and nearshore bathymetry using spaceborne remote sensing: a review. Remote Sens. 11. https://doi.org/10.3390/rs11192212.
Sallenger, J., 2000. Storm impact scale for barrier islands. J. Coast Res. 16, 890–895.
Schumann, G.J.-P., Bates, P.D., 2018. The need for a high-accuracy, open-access global DEM. Front. Earth Sci. 6, 1–5. https://doi.org/10.3389/feart.2018.00225.
Sepúlveda, I., Tozer, B., Haase, J.S., Liu, P.L.F., Grigoriu, M., 2020. Modeling uncertainties of bathymetry predicted with satellite altimetry data and application to tsunami hazard assessments. J. Geophys. Res. Solid Earth 125, 1–25. https://doi.org/10.1029/2020JB019735.
Serafin, K.A., Ruggiero, P., Barnard, P.L., Stockdon, H.F., 2019. The influence of shelf bathymetry and beach topography on extreme total water levels: linking large-scale changes of the wave climate to local coastal hazards. Coast. Eng. 150, 1–17. https://doi.org/10.1016/j.coastaleng.2019.03.012.
Shi, W.Z., Li, Q.Q., Zhu, C.Q., 2005. Estimating the propagation error of DEM from higher-order interpolation algorithms. Int. J. Rem. Sens. 26, 3069–3084. https://doi.org/10.1080/01431160500057905.
Shi, W.Z., Wang, B., Tian, Y., 2014. Accuracy analysis of digital elevation model relating to spatial resolution and terrain slope by bilinear interpolation. Math. Geosci. 46, 445–481. https://doi.org/10.1007/s11004-013-9508-8.
Short, A., 2022. Sediment size dataset for Australia. Australian Coastal Systems. Springer Cham. https://doi.org/10.5281/zenodo.7127184.
Simpson, A.L., Balog, S., Moller, D.K., Strauss, B.H., Saito, K., 2015. An urgent case for higher resolution digital elevation models in the world's poorest and most vulnerable countries. Front. Earth Sci. 3, 50. https://doi.org/10.3389/feart.2015.00050.
Smith, S., Holland, D., Longley, P.A., 2004. The importance of understanding error in Lidar digital elevation models. Int. Arch. Photogramm. Remote Sens. Spat. Inf. Sci. 35, 996–1001.

Smith, W.H.F., Sandwell, D.T., 1997. Global sea floor topography from satellite altimetry and ship depth soundings. Science 277, 1956–1962. https://doi.org/10.1126/science.277.5334.1956.
Smith, W.H.F., Sandwell, D.T., 1994. Bathymetric prediction from dense satellite altimetry and sparse shipboard bathymetry. J. Geophys. Res. 99. https://doi.org/10.1029/94jb00988.
Soulsby, R.L., 1997. Dynamics of marine sands: a manual for practical applications. Oceanogr. Lit. Rev. 9, 947.
Splinter, K.D., Turner, I.L., Davidson, M.A., Barnard, P., Castelle, B., Oltman-Shay, J., 2014. A generalized equilibrium model for predicting daily to interannual shoreline response. J. Geophys. Res. Earth Surf. 119, 1936–1958. https://doi.org/10.1002/2014JF003106.
Tadono, T., Ishida, H., Oda, F., Naito, S., Minakawa, K., Iwamoto, H., 2014. Precise global DEM generation by ALOS PRISM. ISPRS Ann. Photogramm. Remote Sens. Spat. Inf. Sci. II–4, 71–76. https://doi.org/10.5194/isprsannals-ii-4-71-2014.
Tadono, T., Nagai, H., Ishida, H., Oda, F., Naito, S., Minakawa, K., Iwamoto, H., 2016. Generation of the 30 M-MESH global digital surface model by alos prism. Int. Arch. Photogramm. Remote Sens. Spat. Inf. Sci. - ISPRS Arch. 41, 157–162. https://doi.org/10.5194/isprsarchives-XLI-B4-157-2016.
Takaku, J., Tadono, T., Doutsu, M., Ohgushi, F., Kai, H., 2020. Updates of "AW3D30" ALOS global digital surface model with other open access datasets. Int. Arch. Photogram. Rem. Sens. Spatial Inf. Sci. 43, 183–190. https://doi.org/10.5194/isprs-archives-XLIII-B4-2020-183-2020.
Thierry, S., Dick, S., George, S., Benoit, L., Cyrille, P., 2019. EMODnet bathymetry a compilation of bathymetric data in the European waters. Ocean. 2019 - Marseille. https://doi.org/10.1109/OCEANSE.2019.8867250, 2019-June.
Torresan, S., Critto, A., Dalla Valle, M., Harvey, N., Marcomini, A., 2008. Assessing coastal vulnerability to climate change: comparing segmentation at global and regional scales. Sustain. Sci. 3, 45–65. https://doi.org/10.1007/s11625-008-0045-1.
Tozer, B., Sandwell, D.T., Smith, W.H.F., Olson, C., Beale, J.R., Wessel, P., 2019. Global bathymetry and topography at 15 arc sec: SRTM15+. Earth Sp. Science 6, 1847–1864. https://doi.org/10.1029/2019EA000658.
Tseng, K.H., Kuo, C.Y., Lin, T.H., Huang, Z.C., Lin, Y.C., Liao, W.H., Chen, C.F., 2017. Reconstruction of time-varying tidal flat topography using optical remote sensing imageries. ISPRS J. Photogrammetry Remote Sens. 131, 92–103. https://doi.org/10.1016/j.isprsjprs.2017.07.008.
Turner, I.L., Leaman, C.K., Harley, M.D., Thran, M.C., David, D.R., Splinter, K.D., Matheen, N., Hansen, J.E., Cuttler, M.V.W., Greenslade, D.J.M., Zieger, S., Lowe, R. J., 2024. A framework for national-scale coastal storm hazards early warning. Coast. Eng. 192, 104571. https://doi.org/10.1016/j.coastaleng.2024.104571.
Uttenthaler, A., Barner, F., Hass, T., Makiola, J., D'Angelo, P., Reinartz, P., Carl, S., Steiner, K., 2013. Euro-Maps 3D – a Transnational, High-Resolution Digital Surface Model for Europe, SP-722. Spec. Publ.
Uuemaa, E., Ahi, S., Montibeller, B., Muru, M., Kmoch, A., 2020. Vertical accuracy of freely available global digital elevation models (Aster, aw3d30, merit, tandem-x, srtm, and nasadem). Remote Sens. 12, 1–23. https://doi.org/10.3390/rs12213482.
Varner, J.D., Cartwright, J., Rosenberg, A.M., Amante, C., Sutherland, M., Jencks, J.H., 2017. New Multibeam Bathymetry Mosaic at NOAA/NCEI, vol. 2017. AGU Fall Meet. Abstr.. OS41A-1371.
Vassilaki, D.I., Stamos, A.A., 2020. TanDEM-X DEM: comparative performance review employing LIDAR data and DSMs. ISPRS J. Photogrammetry Remote Sens. 160, 33–50. https://doi.org/10.1016/j.isprsjprs.2019.11.015.
Vousdoukas, M.I., Bouziotas, D., Giardino, A., Bouwer, L.M., Mentaschi, L., Voukouvalas, E., Feyen, L., 2018. Understanding epistemic uncertainty in large-scale coastal flood risk assessment for present and future climates. Nat. Hazards Earth Syst. Sci. 18, 2127–2142. https://doi.org/10.5194/nhess-18-2127-2018.
Vousdoukas, M.I., Clarke, J., Ranasinghe, R., Reimann, L., Khalaf, N., Duong, T.M., Ouweneel, B., Sabour, S., Iles, C.E., Trisos, C.H., Feyen, L., Mentaschi, L., Simpson, N.P., 2022. African heritage sites threatened as sea-level rise accelerates. Nat. Clim. Change 12, 256–262. https://doi.org/10.1038/s41558-022-01280-1.
Vousdoukas, M.I., Ranasinghe, R., Mentaschi, L., Plomaritis, T.A., Athanasiou, P., Luijendijk, A., Feyen, L., 2020. Sandy coastlines under threat of erosion. Nat. Clim. Change 10, 260–263. https://doi.org/10.1038/s41558-020-0697-0.
Vousdoukas, M.I., Voukouvalas, E., Mentaschi, L., Dottori, F., Giardino, A., Bouziotas, D., Bianchi, A., Salamon, P., Feyen, L., 2016. Developments in large-scale coastal flood hazard mapping. Nat. Hazards Earth Syst. Sci. Discuss 0, 1–24. https://doi.org/10.5194/nhess-2016-124.
Vrdoljak, L., 2021. Comparison and analysis of publicly available bathymetry models in the east adriatic sea. Nase More 68, 110–119. https://doi.org/10.17818/NM/2021/2.7.
Weatherall, P., Marks, K.M., Jakobsson, M., Schmitt, T., Tani, S., Arndt, J.E., Rovere, M., Chayes, D., Ferrini, V., Wigley, R., 2015. A new digital bathymetric model of the world's oceans. Earth Sp. Science 2, 331–345. https://doi.org/10.1002/2015EA000107.
Wechsler, S.P., 2007. Uncertainties associated with digital elevation models for hydrologic applications: a review. Hydrol. Earth Syst. Sci. 11, 1481–1500. https://doi.org/10.5194/hess-11-1481-2007.
Wendleder, A., Wessel, B., Roth, A., Breunig, M., Martin, K., Wagenbrenner, S., 2012. TanDEM-X water indication mask: generation and first evaluation results. IEEE J. Sel. Top. Appl. Earth Obs. Rem. Sens. 6, 171–179. https://doi.org/10.1109/JSTARS.2012.2210999.
Wentworth, C.K., 1922. A scale of grade and class terms for clastic sediments. J. Geol. 30, 377–392.
Wernette, P., Houser, C., Bishop, M.P., 2016. An automated approach for extracting Barrier Island morphology from digital elevation models. Geomorphology 262, 1–7. https://doi.org/10.1016/j.geomorph.2016.02.024.
Wessel, B., 2018. TanDEM-X ground segment - DEM products specification document. EOC, DLR, Oberpfaffenhofen, Ger. Public Doc. TD-GS-PS-0 49.
Wessel, B., Huber, M., Wohlfart, C., Marschalk, U., Kosmann, D., Roth, A., 2018. Accuracy assessment of the global TanDEM-X digital elevation model with GPS data. ISPRS J. Photogrammetry Remote Sens. 139, 171–182. https://doi.org/10.1016/j.isprsjprs.2018.02.017.
Whiteway, T.G., 2009. Australian Bathymetry and Topography Grid, June 2009. Geoscience Australia. https://doi.org/10.4225/25/53D99B6581B9A.
Wiegmann, N., Perluka, R., Boogaard, K., 2002. Onderzoek Naar Efficiency Verbetering Kustlodingen, RIKZ. Rijkswaterstaat.
Wölfl, A.C., Snaith, H., Amirebrahimi, S., Devey, C.W., Dorschel, B., Ferrini, V., Huvenne, V.A.I., Jakobsson, M., Jencks, J., Johnston, G., Lamarche, G., Mayer, L., Millar, D., Pedersen, T.H., Picard, K., Reitz, A., Schmitt, T., Visbeck, M., Weatherall, P., Wigley, R., 2019. Seafloor mapping - the challenge of a truly global ocean bathymetry. Front. Mar. Sci. 6, 1–16. https://doi.org/10.3389/fmars.2019.00283.
Xu, N., Ma, Y., Yang, J., Wang, X.H., Wang, Y., Xu, R., 2022. Deriving tidal flat topography using ICESat-2 laser altimetry and sentinel-2 imagery. Geophys. Res. Lett. 49, 1–10. https://doi.org/10.1029/2021GL096813.
Yamaguchi, Y., Kahle, A.B., Tsu, H., Kawakami, T., Pniel, M., 1998. Overview of advanced spaceborne thermal emission and reflection radiometer (ASTER). IEEE Trans. Geosci. Rem. Sens. 36, 1062–1071. https://doi.org/10.1109/36.700991.
Zhang, K., Gann, D., Ross, M., Biswas, H., Li, Y., Rhome, J., 2019. Comparison of TanDEM-X DEM with LiDAR data for accuracy assessment in a coastal urban area. Remote Sens. 11. https://doi.org/10.3390/RS11070876.